Hydrodynamic loading of breaking waves of breaking waves on offshore inspection platforms

Thesis

By

David Pavilons

Master of Science

in Marine technology
at the Delft university of Technology

Student:	David Pavilons
Chair supervisor:	Peter Wellens
University committee 1:	Bas Hofland
University committee 2:	Martin van der Eijk
Company supervisor:	Désirée Plenker
Company supervisor:	Niek Bruinsma
Company team member:	Vera Hengelmolen

Graduation date: 15-12-2022

Delft University of Technology

Deltares
Enabling Delta Life

Hydrodynamic loading of breaking waves on offshore inspection platforms

David Pavilons, Désirée Plenker, Niek Bruinsma, Vera Hengelmolen, Luc Biermans, Alfons Smale and Peter Wellens

Delft University of Technology, Deltares
Faculty of Mechanical, Maritime and Materials Engineering, 3mE
Thesis, MT.22/23.016.M.

December 9, 2022

The most violent breaking waves cause the largest platform forces at sea, however it is unknown which wave in a sea state leads to these forces if run-up is included. Offshore inspection platforms give access to wind turbine monopiles. They are positioned above mean sea level. Wave interaction with monopiles leading to run-up causes vertical impact forces on inspection platforms. Predicting the vertical impact is challenging. The objective of this article is to find the wave in a sea state that causes the largest vertical impact force on a horizontal platform. It is hypothesized that breaking waves will cause the largest vertical forces. Detailed numerical OpenFOAM Volume-of-Fluid simulations are performed to investigate wave breaking interaction with structures. long-crested wave propagation was considered in 2D with a schematized inspection platform, composed of a horizontal deck and a vertical wall above mean sea level – the minimum requirements to still cause wave run-up and a vertical impact. This simplified numerical setup results in high resolution particle velocities that we require for further investigation with the kinematic breaking criterion. A potential flow solver, OceanWave3D, was used to generate a three-hour sea state representative of North Sea conditions. From the sea state, 17 waves were selected based on the kinematic breaking criterion and their surface elevation. The selected waves were fed into an OpenFOAM domain with and without structure to determine their breaking index, particle velocities and forces on the structure. This is the first study to use the breaking index as a screening parameter for critical wave selection. The three waves causing the largest forces on the structure were simulated again with the structure present at various horizontal positions relative to the point of wave overturning. The wave with the highest surface elevation and the highest breaking index overturning one third of the peak wave length before the inspection platform caused the largest vertical forces. This is due to the strong relation between impacts loads and the free surface particle velocity

1 Introduction

It is estimated that there will be a total number of $30,000$ wind turbines installed by 2030 globally (Gourvenec and Sykes, 2021). This prediction is a positive development for the offshore wind business and the global need for green energy. However, the knowledge about wave interaction with monopiles is still incomplete as reported damage to inspection platforms demonstrates that the predicted impact forces were exceeded, see Figure 1 (Damsgaard, Gravesen, and Andersen, 2007).

Figure 1: Wave run-up at Horns Reef (Damsgaard, Gravesen, and Andersen, 2007)

Estimated source of problem due to breaking waves

Monopiles are mostly located in intermediate water depths. Therefore, depth-induced wave breaking may occur due to the specific bathymetry (Aggarwal et al., 2020). From literature (Tang et al., 2020), it is known that breaking waves have larger hydrodynamic loads compared to non-breaking waves . Based on these references, it is hypothesized that the largest hydrodynamic loads are caused by breaking waves.

Waves breaking is caused due to focusing and bathymetry

Wave breaking in literature is discussed in relation to depth-induced breaking and wave focusing. Depth-induced breaking in irregular waves is too complex to capture by means of simple geometric properties (Aggarwal et al., 2020). Wave breaking might occur in irregular waves due to the effect of focusing. Focusing can occur when two wave groups cross each other at specific angles and produce a vertical upward jet McAllister et al., 2018. Crossing wave groups could be the mechanism behind the Draupner freak wave event, which inflicted damage to the Draupner platform. Less nonlinear is the energy transfer and subsequent breaking during unidirectional focusing when wave components are created in such a way that they are in phase at a specific location. This is described in more detail in Bos and Wellens, 2021, presenting a method that uses discrete wave packets of different frequency to create a focused breaking wave. Alberello and Iafrati, 2019 found that simulations underpredict the velocity close to the wave crest compared to measurements. Higher resolutions seem necessary in order to capture the most relevant details of the flow.

Explanation need for new kinematic breaking criterion

Monopiles are subject to irregular waves. Wave breaking in irregular waves can best be described with a unified breaking criterion. The kinematic breaking criterion states that if the horizontal particle speed is at 85% of the wave speed, the wave will surely break (Barthelemy et al., 2018). Derakhti, Banner, and Kirby, 2018 further investigated the kinematic breaking criterion and found that the breaking strength can be quantified by taking the time derivative of the kinematic breaking criterion. Craciunescu and Christou, 2020 later discussed that their results where in good agreement with the breaking strength definition according to Barthelemy et al., 2018. Craciunescu and Christou, 2020 also found that focused breaking waves lose less than 20% of their energy during breaking. The kinematic breaking criterion was investigated further by Varing et al., 2021, contributing that the vector norm of the particle velocity leads to better results compared to using only the horizontal component of the particle velocity at the free surface.

Relation monopile inline forces and wave breaking

As the wave breaks, it first hits the monopile before reaching the inspection platform. While the knowledge of vertical wave impact forces on inspection platforms is incomplete (Bredmose and Jacobsen, 2011), the knowledge of inline wave forces on monopiles is also not entirely understood. Paulsen et al., 2019 were not able to formulate an all-encompassing relation between surface elevation and inline forces; in defining the slamming coefficient they found that waves with smaller wave height may lead to larger forces than waves with larger wave height. In Tai et al., 2019 for monopiles and Bos and Wellens, 2021 for a horizontal cylinder that was free to move, it was found that there is a significant difference in monopile inline forces in breaking waves for different relative structure positions compared to the point of wave overturning.

Monopile impacts leading to wave run-up

Wave interaction with monopiles on many occasion leads to wave run-up. PENG, Wellens, and Raaijmakers, 2012, did a study on the comparison between a CFD model and the results of Damsgaard, Gravesen, and Andersen, 2007 and found that wave run-up is strongly dependant on the wave nonlinearity. Ramirez et al., 2013 improved the formulations of Damsgaard, Gravesen, and Andersen, 2007 and observed that there was no significant difference for model tests at different scale. Garborg et al., 2019 performed a meta-analysis of the existing literature and confirmed that steep nonlinear waves produce the highest run-up. A recent publication, Grue and Osyka, 2021, found that the highest run-up was achieved when the wave breaks violently just behind the monopile. One of the latest developments in monopile foundation structures is the composite bucket foundation (CBF). However, this structure lead to larger run-up compared to standard monopile foundations structures. This may be due to the arc transition piece which retains the water particle kinetic energy Zhang, Yu, and Zhao, 2022.

Literature platform impacts due to run-up is lacking

Literature exists on platform loads due to run-up, but the exact relationships between wave breaking kinematics and impact loads is unknown. Experimental investigation of irregular wave interaction with a monopile and inspection platform was done by Andersen, Lykke, and Brorsen, 2007. They observed that irregular and potentially breaking waves caused more slamming compared to regular waves. Damsgaard, Gravesen, and Andersen, 2007 discovered that loads on a horizontal platform were twice as high compared to a conical platform with a bottom slope of 45 degrees. Additionally they concluded that the loads on a porous platform were up to 70% smaller compared to closed platforms. Large scale model tests of impact forces in irregular waves are described in Andersen et al., 2011. The associated loads were highly sensitive to the detailed wave breaking kinematics. A numerical investigation of wave interaction with a monopile and an inspection platform was performed by Bredmose and Jacobsen, 2011. It was found that the lowest platform elevation resulted in the highest forces. They also mentioned that the point of wave overturning was influenced by the grid resolution. Almeida and Hofland, 2021 did an analysis on standing wave impacts on a vertical hydraulic structures with overhangs. They observed that irregular wave impacts had a large range of different time dependent load curves. The setup used by Almeida and Hofland, 2021 is similar to a setup with the cross-section of a monopile with an inspection platform. The amount of reflection for walls with overhangs, however, would be unrealistic for monopiles.

Up to date platform literature exists without monopile

There is recent literature on the interaction between extreme waves and structures above the mean waterline, but these neglect the run-up on the monopile. Stansberg, 2020 and Bunnik, Scharnke, and Ridder, 2019 both concluded that the wave growth rate $d\eta/dt$ was a reasonable approach for sea state screening of wave-in-deck slamming loads for a fixed structure. Moideen et al., 2020 and Filip, Xu, and Maki, 2020 both left out the structure beneath the offshore platform and considered wave interaction with the platform in 2D. Filip, Xu, and Maki, 2020 again found that the force on the platform is related to the wave steepness. Moideen et al., 2020 observed that breaking waves lead to vertical forces two times larger than non-breaking waves. With the freely suspended horizontal cylinder in Bos and Wellens, 2021 it was found that an aerated wave impact after breaking lead to more energy transfer compared to a flip-through impact.

Problem analysis

The largest force on a platform without foundation structure is caused by plunging breaking waves Moideen et al., 2020, while the largest run-up is achieved if the wave breaks violently behind the monopile Grue and Osyka, 2021. However, the existing literature is inconclusive about which wave in a sea state leads to the largest hydrodynamic load on an offshore inspection platform.

Objective research

This research tries to find the mechanism behind vertical wave loads on inspection platforms during wave interaction with a single wave in long-crested wave propagation. The effects of wave crossing and wave reflection are left out by carefully designing the platform undergoing the load. The focus of the research is on the relation between wave parameters and the inspection platform loads, leading to the objective which is to select the wave from a sea state that leads to the largest vertical wave load on a inspection platform. When formulated as a research question, it reads:

Which wave from a sea state leads to the largest hydrodynamic loads on a monopile inspection platform?

The research question has two main aspects, which, when formulated as sub-questions, are:

- Which waves lead to the largest hydrodynamic loads?
- How does the position of the structure, with respect to a representative location in the breaking wave, influence the hydrodynamic loads?

Theoretical approach and it's novelties
We choose to adopt a numerical approach so that it is possible to obtain high-resolution kinematic data together with the details of the free surface at every horizontal position. The waves are considered to be long-crested and the numerical domain is chosen to be two-dimensional (2D). Commonly used wave parameters such as wave height and wave steepness are used to select waves, but also the updated breaking criterion presented in Varing et al., 2021 is investigated. For the investigation a new method for calculating the global crest speed in irregular waves is developed. Our study is the first to consider breaking index and breaking strength (Derakhti, Banner, and Kirby, 2018) as a screening method to find the waves in a sea state that lead to the largest hydrodynamic force on a structure. In order to focus on the parts of monopile and inspection platform that induce the essential mechanisms leading to a vertical load on the platform, the structure is modelled as an inverted L as such: Ꞁ and positioned at various locations with respect to the incipient point of breaking, where the wave starts to overturn. The effects of air compression, friction and turbulence are neglected as they are a matter of further research. Hence the investigation is done numerically.

Reading guide
section 2 describes the numerical setup of this research with a potential flow solver for wave propagation that feeds time signals with the kinematics of the selected wave to the Volume-of-Fluid (VOF) solver. A new method for determining single wave breaking events and a method for calculating the global wave crest speed is described in section 3. Results of wave propagation in both the potential flow solver and the VOF solver are shown in section 4. The relation between wave parameters and hydrodynamic loading on offshore platforms is elaborated upon in section 5, after which the main conclusions are summarized in section 6.

2 Numerical approach

The problem of wave interaction with the offshore inspection platform is solved numerically. The numerical domain consists of a fully nonlinear potential flow solver coupled with a fully nonlinear Navier–Stokes volume of incompressible fluid method. The outer domain is modeled with OceanWave3D (Engsig-Karup, Bingham, and Lindberg, 2009), the inner domain is modeled with OpenFOAM (Jacobsen, Fuhrman, and Fredsøe, 2012). The coupling method used between the two models is described in Paulsen, Bredmose, and Bingham, 2014. A sketch of the numerical domain including the 2D representation of the structure, Ꞁ is seen in Figure 2.

2.1 Governing equations Potential flow solver

The wave propagation simulations in OceanWave3D are done in 2D with irrotational and incompressible flow. The velocity potential relates to the fluid velocities in the following way

$$\mathbf{u} = \nabla \cdot \phi, \tag{1}$$

with ϕ being the velocity potential, the velocity vector $\mathbf{u}$ and the and the nabla operator, ∇ relate to the horizontal and vertical fluid velocities the following way

$$\mathbf{u} = (u_x, u_z)\,, \tag{2}$$

$$\nabla = \left(\frac{\partial}{\partial x}, \frac{\partial}{\partial z}\right). \tag{3}$$

This leads to the kinematic free surface condition (Paulsen, Bredmose, and Bingham, 2014), which is stated as

$$\frac{\partial \eta}{\partial t} = -\frac{\partial \eta}{\partial x}\frac{\partial \tilde{\phi}}{\partial x} + \frac{\partial \tilde{\phi}}{\partial z}\left(1 + \left(\frac{\partial \eta}{\partial x}\right)^2\right), \tag{4}$$

with η the free surface elevation and t the time. The velocity potential at the free surface is described with

$$\tilde{\phi} = \phi|_{z=\eta}\,. \tag{5}$$

The dynamic free surface condition reads (Paulsen, Bredmose, and Bingham, 2014)

$$\frac{\partial \tilde{\phi}}{\partial t} = -g\eta - \frac{1}{2}\left(\left(\frac{\partial \tilde{\phi}}{\partial x}\right)^2 - \left(\frac{\partial \tilde{\phi}}{\partial z}\right)^2\left(1 + \left(\frac{\partial \eta}{\partial x}\right)^2\right)\right), \tag{6}$$

with g the acceleration of gravity. The bathymetry has a no penetration boundary condition.

Problems with mathematical description
As the wave approaches it's overturning point, the wave front becomes steeper. This means the local wave steepness, ($\frac{d\eta}{dx}$) approaches negative infinity prior to the point of overturning. This generates an infinite surface elevation growth rate $\left(\frac{d\eta}{dt}\right)$. Mathematically this is formulated as

$$\lim_{\frac{d\eta}{dx}\to-\infty} \frac{d\eta}{dt}\left(\frac{d\eta}{dx}\right) = \infty\frac{\partial \tilde{\phi}}{\partial x} + \infty^2\frac{\partial \tilde{\phi}}{\partial z}. \tag{7}$$

Description breaking filter for continuous computations
OceanWave3D uses a filter to assure that surface elevation growth rate values do not approach infinity. If the following condition is met $\frac{\partial w}{\partial t} < -\gamma g$, a compact spatial Savitzky–Golay filter is applied for local energy removal, with $\gamma \in [0.5; 1]$ being a user defined parameter. This filter is not accurate for wave overturning, but it guarantees continuous computation beyond a breaking event (Paulsen, Bredmose, and Bingham, 2014).

2.2 Governing equations VOF solver

OceanWave3D is coupled with an in inner domain which is able to simulate wave breaking. This inner domain is setup with the Wave2Foam OpenFOAM volume-of-Fluid solver toolbox

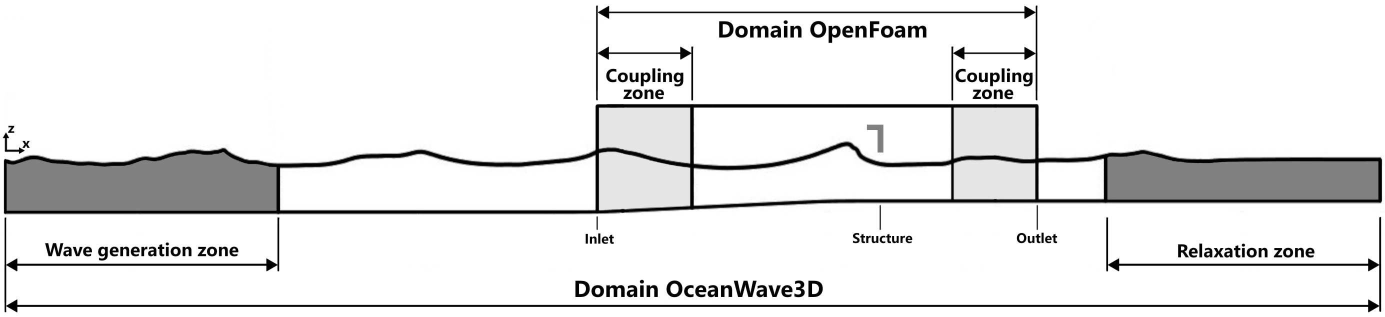

Figure 2: Sketch numerical wave tank

(Jacobsen, Fuhrman, and Fredsøe, 2012). The fluid is modeled as an incompressible two-phase flow with the respective conservation of mass equation.

$$\nabla \cdot \mathbf{u} = 0. \tag{8}$$

OpenFOAM makes no distinction between 2D and 3D simulations. Therefore the velocity components **u** and the ∇ operator are stated as (Jacobsen, Fuhrman, and Fredsøe, 2012)

$$\mathbf{u} = (u_x, u_y, u_z), \tag{9}$$

$$\nabla = \left(\frac{\partial}{\partial x}, \frac{\partial}{\partial y}, \frac{\partial}{\partial z} \right). \tag{10}$$

Since this setup is done in 2D, the results in y-direction are neglected. The conservation of momentum equation states

$$\frac{\partial \rho \mathbf{u}}{\partial t} + \nabla \cdot (\rho \mathbf{u})\mathbf{u}^T = \nabla p^* - (\mathbf{g} \cdot \mathbf{x})\nabla \rho, \tag{11}$$

u and **x** are the fluid velocity and position vectors, while ρ stands for the fluid density. In Equation 11 it is seen that the physical viscosity is neglected, therefore only numerical viscosity is present. The modified pressure, p^* is defined as

$$p^* = p - \rho \mathbf{g} \cdot \mathbf{x}, \tag{12}$$

Here, p is the total pressure. The local fluid density ρ is defined by the scalar water volume fraction α, which has the following relation with the local volume density

$$\rho = \alpha \rho_w + \rho_a (1 - \alpha). \tag{13}$$

The subscripts w and a stand for water and air. After solving for the velocity field, α is computed from

$$\frac{\partial \alpha}{\partial t} + \nabla \cdot \mathbf{u}\alpha + \nabla \cdot u_r \alpha (1 - \alpha) = 0. \tag{14}$$

The relative compression term u_r is used on the free surface to remove nonphysical values. A more detailed explanation of the governing equations is given in Jacobsen, Fuhrman, and Fredsøe, 2012.

2.3 Boundary conditions

The two solvers are coupled at two different locations. There is coupling at the inlet and at the outlet zone. This implies that both coupling zones in OpenFOAM have a target wave that comes from the simulations in OceanWave3D. Within the coupling zones the free surface elevation and the particle velocities are relaxed for each time step with the following equations

$$\begin{aligned} \eta(x,t) &= \xi(\sigma)\eta_{target}(x,t) + (1 - \xi(\sigma))\eta(x,t)_{computed}, \\ \mathbf{u}(x,t) &= \xi(\sigma)\mathbf{u}_{target}(x,t) + (1\xi(\sigma))\mathbf{u}(x,t)_{computed}, \end{aligned} \tag{15}$$

preventing reflection of structure-induced disturbances at domain walls. The relaxation factor $\xi(\sigma)$ is defined as

$$\xi(\sigma) = 1 - \frac{exp(\sigma^{3.5} - 1)}{exp(1) - 1}, \quad \sigma\,[0,1], \tag{16}$$

with σ the normalized horizontal coordinate along the coupling zone. The value is zero at the location of the inlet and outlet, while the value is one at the boundary between the coupling zones and the inner OpenFoam domain. A representation of the coupling zones is seen in Figure 2.

Boundary conditions Oceanwave3D

The OceanWave3D boundary conditions are setup with a wave generation zone and a relaxation zones (Engsig-Karup, Bingham, and Lindberg, 2009). The wave generation zone produces a sea state based on a chosen JONSWAP spectrum. Due to the bathymetry of the setup, waves reflected towards the wave generation zone are removed by the relaxation technique (Paulsen, Bredmose, and Bingham, 2014). Wave reflection due to the finite length of the domain is removed with a relaxation zone at the end of the domain. To guarantee effective simulations, the wave generation and relaxation zone demand a range longer than one peak wave length. The zones are depicted in Figure 2.

Boundary conditions OpenFOAM

The inner OpenFoam boundary conditions have a simplified setup to guarantee a short simulation duration. The boundary conditions for the bathymetry and the structure are set at a slip and no penetration boundary condition, as friction is neglected in this study. The pressures for the bottom, inlet and outlet have a zero-gradient boundary condition while the top of the domain has an atmospheric pressure. Since there is no friction with the sea wall and turbulence is turned off, the fluids particles only endure numerical energy dissipation. This leads to larger velocities at the sea wall compared to physical experiments, these effects are a matter of further research.

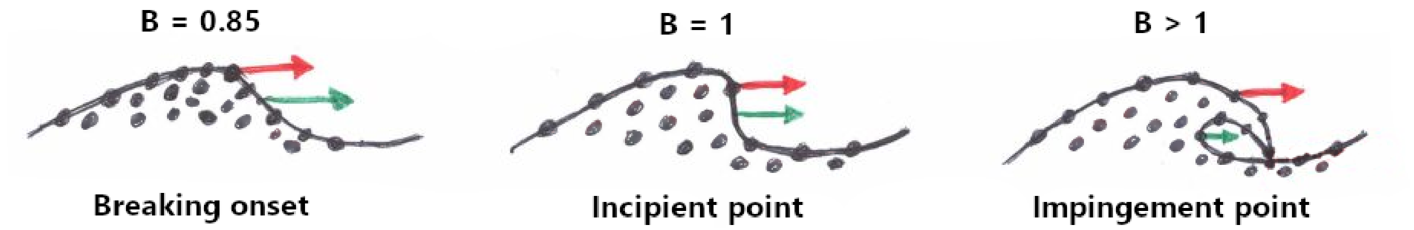

Figure 3: Critical wave moments in time

3 State of the art wave breaking formulations

A wave has three critical moments in time: Breaking onset (Barthelemy et al., 2018), the incipient point and the impingement point (Ma et al., 2020). The breaking onset is defined as the point of no return, after which breaking is inevitable (Barthelemy et al., 2018); the incipient point is defined as the point where wave overturning starts and where the wave front is vertical (Ma et al., 2020); the impingement point is defined as the location where the wave crest hits the water surface. These critical moments are quantified with the kinematic breaking criterion B as stated in Barthelemy et al., 2018 and improved by Varing et al., 2021. Varing et al., 2021 define the kinematic breaking criterion as

$$B = \frac{||\mathbf{u}||_m}{C_x}. \tag{17}$$

Here, $||\mathbf{u}_m||$ is defined as the maximum occurring free surface particle velocity magnitude,

$$||\mathbf{u}||_m = max\left(\sqrt{u_x^2 + u_y^2}\right). \tag{18}$$

The symbols u_x and u_y stand for the horizontal and vertical free surface velocity. The wave speed, C_x is described with the linear dispersion relation

$$C_x = \sqrt{\frac{g \cdot tanh(k \cdot h(x))}{k}}. \tag{19}$$

The water depth $h(x)$ depends on the bathymetry and the wave number k. The wave number k relates to the wave speed as follows

$$k = \frac{\omega}{C_x}, \tag{20}$$

in which ω is the angular wave frequency. The breaking onset is quantified with B being equal to 0.85 (Barthelemy et al., 2018); the incipient point is reached when the kinematic breaking criterion is close to one (Varing et al., 2021); the impingement point (Ma et al., 2020) has a kinematic breaking criterion greater than one, as the particles have overtaken the wave. An overview of these critical moments is shown in Figure 3.

Reading guide

Derakhti, Banner, and Kirby, 2018 discovered a relation between the kinematic breaking criterion and the wave breaking strength. This phenomena is described in subsection 3.1. Subsection 3.2 and subsection 3.3 describe the application of the theory on the results of the numerical methods.

3.1 Breaking index and breaking strength

Breaking index formulation

Derakhti, Banner, and Kirby, 2018 observed a relation between the time derivative of the kinematic breaking criterion and the level to which a wave undergoes plunging breaking. The non-dimensional level of wave breaking is abbreviated to 'breaking index' and reads

$$\Gamma_{wave} = T \cdot \frac{dB}{dt}, \tag{21}$$

with T being the wave period. This research further enhances the method by inserting Equation 17 into Equation 17, as Derakhti, Banner, and Kirby, 2018 used the horizontal particle velocity instead of the magnitude.

Breaking acceleration formulation

The breaking index not intuitive, and is better understood if it's dimensional form is multiplied by the wave speed. This results in a formulation of breaking acceleration

$$C_x \frac{\partial B}{\partial t} = \frac{d||\mathbf{u}||_m}{dt} - B\frac{dC_x}{dt}. \tag{22}$$

Equation 22 implies that the water particle acceleration minus the wave acceleration times the kinematic breaking criterion is equal to the breaking acceleration. Thus if water particles accelerate and the wave crest decelerates, the wave experiences positive wave breaking acceleration. The exact relation between wave loads on structures and wave breaking acceleration is a matter of further research.

Breaking strength as defined in literature

Derakhti, Banner, and Kirby, 2018 found a relation between the breaking strength (ϵ) and the breaking index evaluated at $B_x = 0.85$. The breaking strength, or wave energy dissipation rate per unit area of wave, was defined in Duncan, 1983 as

$$\epsilon = b \cdot \rho \frac{C_x^5}{g}. \tag{23}$$

Here, ρ equals the fluid density, g the gravitational acceleration, C_x the crest speed, and b a dimensionless constant, also known as the breaking strength parameter. Derakhti, Banner, and Kirby, 2018 found the following empirical relation for b

$$b = 0.034\left(\Gamma_{wave} - 0.3\right)^{2.5}. \tag{24}$$

A minimum breaking index of 0.3 is needed for this formulation. Otherwise ϵ and Γ_{wave} are not related.

3.2 Wave breaking OceanWave3D

Defining new breaking onset criterion Oceanwave3D

Equation 17 requires the wave crest speed for breaking onset determination,. This is challenging in a sea state, as different wave components have different velocities. Therefore a local wave speed is determined in OceanWave3D with a local wave number. This is done with a partial Hilbert transform (Kurnia and Groesen, 2014)

$$\mathcal{H}(\eta) = \frac{-1}{\pi} \lim_{\tau \to 0} \int_{\tau}^{\infty} \frac{\eta(x+x') - \eta(x-x')}{x'} dx', \qquad (25)$$

with η the surface elevation. The spatial Hilbert transform is taken with respect to x for each time step. By definition the Hilbert transforms makes a phase angle shift of 90 degrees compared to the original data. Therefore the following relation is derived with the Hilbert transform (Kurnia and Groesen, 2014)

$$tan(\omega) = \frac{\mathcal{H}(\eta)}{\eta}. \qquad (26)$$

This makes the angular wave frequency ω solely dependent on the surface elevation η and therefore independent of time, leading to the rewritten spatial derivative relation

$$\frac{\partial \omega}{\omega x} = \frac{\cos \omega^2}{\eta^2} \left(\eta \frac{\partial \mathcal{H}(\eta)}{\partial x} - \mathcal{H}(\eta) \frac{\partial \eta}{\partial x} \right). \qquad (27)$$

The relation for the local wave number and the cosine function of the angular frequency squared are defined as followes

$$k = \frac{\partial \omega}{\partial x}, \qquad (28)$$

$$\cos \omega^2 = \eta^2 / (\eta^2 + \mathcal{H}^2(\eta)). \qquad (29)$$

By inserting these two relations into Equation 27, the following equation is derived for the local wave number that exclusively depends on η

$$k = \frac{1}{\eta^2 + \mathcal{H}^2(\eta)} \left(\eta \frac{\partial \mathcal{H}(\eta)}{\partial x} - \mathcal{H}(\eta) \frac{\partial \eta}{\partial x} \right). \qquad (30)$$

Equation 30 leads to local wave numbers being defined over the full spatial domain. By inserting Equation 30 into Equation 19, the wave speed is determined for each x coordinate.

Errors and limitations local wave speed

Due to the nature of the Hilbert transform some values for C_x become infinite. These values need to be filtered for the breaking onset determination. Generally this is seen at wave troughs, therefore these values have little influence on the breaking estimation.

Calculation breaking onset Oceanwave3D

OceanWave3D generates a free surface velocity potential and a surface elevation for each time step and x-coordinate. The horizontal particle velocity is determined by taking the partial derivative of $\tilde{\phi}$ in x. The growth rate $d\eta/dt$ is determined by taking the time derivative of the surface elevation. The vertical free surface particle velocity is determined with Equation 5. With the horizontal and vertical components known, the breaking onset is determined with the local wave speed as stated in Equation 17.

Determination Breaking events and breaking index

From OceanWave3D all breaking onset events are determined in the total space and time domain. Since in OceanWave3D wave overturning is approximated Equation 7, a filter is applied to ensure robustness (Paulsen, Bredmose, and Bingham, 2014). This raises questions about the accuracy of results after a breaking event. Therefore, a second filter is placed on the results to determine a single wave breaking event. Below, a description of a breaking onset event is provided, followed by a description of a single wave breaking event and its corresponding breaking index.

Determination breaking event

A wave breaking event is defined by the coordinates x_a and t_a where Equation 17 holds true,

$$B(x,t) > 0.85 \text{ at } \begin{cases} x = x_a \\ t = t_a. \end{cases} \qquad (31)$$

The value x_a is defined as the spatial coordinate of the breaking event and t_a is defined as the time coordinate of the breaking event.

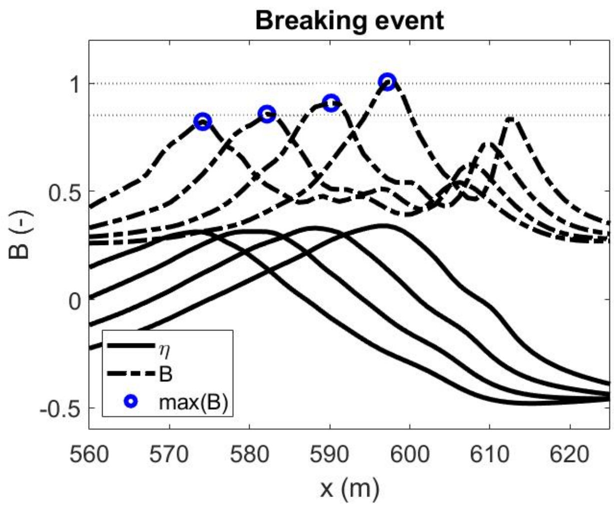

Figure 4: Breaking event oceanwave3D

Figure 4 shows η, B and $max(B)$ for four time steps, η and B at the first time step correspond to the leftmost blue dot for $max(B)$. The surface elevation and breaking criterion data for the fourth time step correspond to the rightmost blue dot. In Figure 4 it is seen that time step one has no breaking events over its x domain. The wave at the second time step has one break event at the blue coordinate. The waves at the third and fourth time step have multiple break events as the blue coordinate only depicts its maximum value.

Determination single Breaking event

A single wave breaking event is here defined as a breaking event without the influence of a previous breaking event for a chosen time and space interval. The following conditions determine a single wave breaking event

$$B(x,t) < 0.85 \text{ at } \begin{cases} x_b < x < x_a \\ t_b < t < t_a. \end{cases} \qquad (32)$$

Equation 32 depends on two user defined parameters x_b and t_b. Parameter x_b is estimated with the corresponding local wave speed,

$$x_b = x_a - C_a \cdot (t_a - t_b), \qquad (33)$$

with C_a being the wave speed at position x_a. This leads to a simplified single wave breaking event condition with one user defined parameter t_a

$$B(x,t) < 0.85 \text{ at } \begin{cases} x_a - C_a \cdot (t_a - t_b) < x < x_a \\ t_b < t < t_a. \end{cases} \qquad (34)$$

Using $t_b = dt \cdot 8$ was found to give good results, with dt being the OceanWave3D time step and dx the OceanWave3D cell size. This is a modeling choice and the influence of the breaking filter as described in Paulsen, Bredmose, and Bingham, 2014 is a matter of further research.

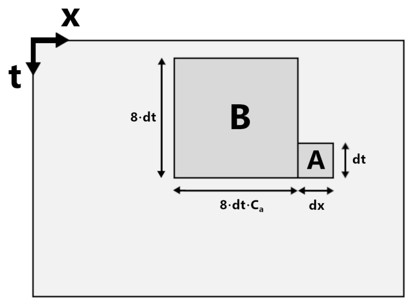

Figure 5: Sketch working mechanism algorithm break events

Figure 5 is a visual representation of Equation 34 in time and space. The coordinates in surface B must satisfy Equation 34. Only then the breaking at x_a can be interpreted as a single wave breaking event according to Equation 31. The second blue dot in Figure 4 depicts a single wave breaking event.

Calculation Breaking index in Oceanwave3D

The breaking index is calculated by taking a linear fit of the maximum occurring B values at each time step. The breaking index is determined with the interpolation range $0.85 < B < 1$. In Figure 4 the second blue dot from the left correspond to a value just above 0.85 and the fourth dot corresponds to a value just above 1. Therefore the dimensional breaking index dB/dt in Figure 4, is calculated by determining the slope between the second and third blue dot in time.

3.3 Wave breaking OpenFoam

Stansell and Macfarlane, 2019 defined three different definitions of wave speed: (i) linear wave theory, (ii) a Hilbert transform and (iii), the speed of a wave crest, all these methods were inconvenient for this setup, therefore a new method is presented (vi), 'the virtual incipient point wave speed', which is a modification of method (iii). The linear wave theory is not applicable for an irregular wave field. Therefore a Hilbert transform is used to define a local wave speed for non-breaking irregular waves (subsection 3.2).

Local wave speed method is not usable in OpenFOAM

A Hilbert transform is a type of Fourier transform and consequently needs evenly distributed coordinates. Since the free surface elevation and particle velocities are extracted with an isosurface at a volume fraction ratio of $\alpha = 0.75$, there are unevenly distributed coordinates. After and at the incipient point, the surface elevation, η has multi-valued x-coordinates. Hence interpolating the surface elevation for evenly distributed coordinates will results in data loss. Therefore determining a Hilbert transform for near-breaking and overturning waves is in this case impossible.

Wave crest tracing is difficult for irregular waves

The method of wave crest tracing was unsuitable as well. The irregular wave field caused locally varying surface elevation peaks at the wave crest. Determining the wave speed by taking the time derivative of the horizontal distance of the highest surface elevation peaks did not lead to the global wave speed. A method is presented for wave speed determination based on the isosurface generated surface elevation. The method performs three actions: (i) the sorting of the surface elevation, (ii) the incipient point determination and (iii), the wave speed determination based on on a virtual incipient point.

Explanation on first step algorithm: sorting

The first step of the algorithm sorts the surface elevation, eta based on a nearest neighbour algorithm with the velocity components indexed correctly. OpenFOAM sorts the isosurface generated surface elevation coordinates beforehand in positive x direction. This results in sorted surface elevation values based on their horizontal coordinate. At wave overturning the surface elevation is a multi valued function of the horizontal position. Hence at wave overturning OpenFOAM does not sort the surface elevation correctly. An algorithm is written which sorts the surface elevation, η for the following condition

$$|\eta^{(i)} - \eta^{(i-1)}| > 0.05m, \tag{35}$$

with $0.05m$ a tuning parameter. This results in the sorting process working solely on places of wave overturning, air bubbles or water droplets. The nearest neighbour algorithm sorts the data based on the following condition

$$min\left(\sqrt{\left(x^{(i)} - x^{(i-1)}\right)^2 + \left(\eta^{(i)} - \eta^{(i-1)}\right)^2}\right), \tag{36}$$

with x and η the horizontal and vertical coordinates of the isosurface. Air bubbles and water droplets are removed in the sorting process.

Explanation on second step algorithm: incipient point

The second step of the algorithm determines the incipient point coordinate (x_{inc}, z_{inc}) with

$$z_{inc} = \eta(x) \text{ at } \frac{d\eta}{dx} > 5, \tag{37}$$

with $d\eta/dx$ the local wave steepness and 5 a tuning parameter. In Figure 6 the incipient point is depicted as the green dot.

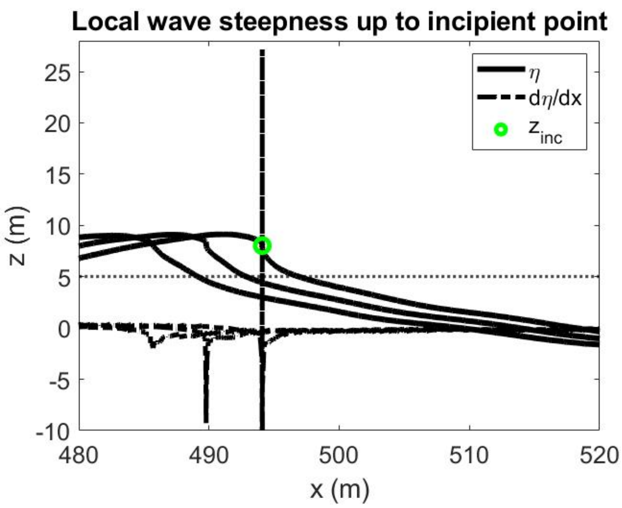

Figure 6: local wave steepness

Explanation on third step algorithm: wave speed

The third step in the algorithm determines the wave speed with the proposed virtual incipient point x_{vinc}

$$C_x^{(n)} = \frac{x_{vinc}^{(n)} - x_{vinc}^{(n-1)}}{dt^{(n)}}, \tag{38}$$

$C_x^{(n)}$ and $x_{vinc}^{(n)}$ stand for the global wave speed and horizontal virtual incipient point coordinate at the current time. The parameter $x_{vinc}^{(n-1)}$ stands for the virtual incipient point at a previous time. The initial condition is known due to step two of the algorithm and is stated as $x_{vinc}^{(0)} = x_{inc}$. The virtual incipient point prior in time $x^{(n-1)}$ is calculated with

$$x_{vinc}^{(n-1)} = max\left(\eta^{(n-1)}(x) \cap z_{inc}\right), \quad \left\{x < x_{vinc}^{(n)}\right\}. \qquad (39)$$

Equation 39 describes that the maximum horizontal intersection value is taken for the crossing between the surface elevation ($\eta^{(n-1)}(x)$) at time $t^{(n-1)}$ and the vertical incipient point height (z_{inc}), provided that the horizontal intersection value $x_{vinc}^{(n-1)}$ at time $t^{(n-1)}$, is lower than the current the horizontal coordinate $x_{vinc}^{(n)}$ at the current time $t^{(n)}$. The Virtual incipient points are linearly interpolated from an upper and lower nearest data point. With the horizontal coordinate known, the wave speed is calculated by inserting Equation 39 into Equation 38. In Figure 7 the method is visualized with the free surface contour at different times. The green dots correspond to the virtual incipient points at each time interval.

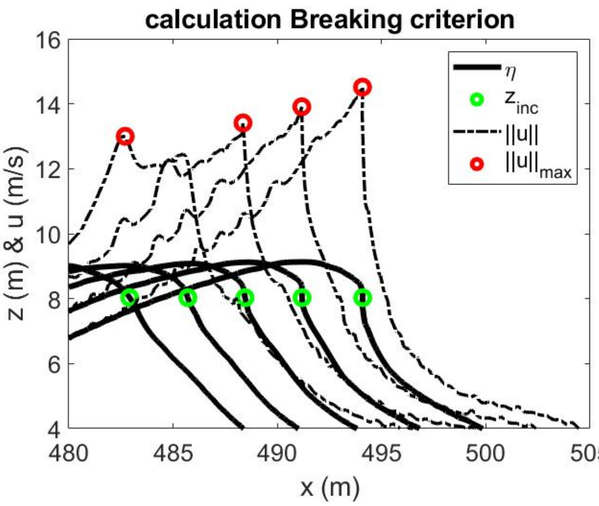

Figure 7: Data points needed for calculating breaking criterion

Particle speed determination

The particle velocities are taken at the positions of an isosurface interpolated at $\alpha = 0.75$ as it gave the least velocity data noise. In Figure 7 the dashed line stands for the magnitude of the particle velocities while the red dots corresponds to its maximum values.

Determination Breaking index

A visualization of the kinematic breaking criterion and breaking index are shown in Figure 8, with the green dots the global wave speed as depicted in Figure 7, the red dots the maximum particle velocities as depicted in Figure 7, the blue dots are the kinematic breaking criterion values as determined in Equation 17. The breaking index dB/dt is determined by taking a linear-fit of the time derivative of B, for a range between B>0.9 and the incipient point. This is depicted as the black line in Equation 17.

Explanation on verification breaking method

Varing et al., 2021 observed a point of wave overturning at a value of $B = 1.05$. They considered $||u||_m/c \approx 1$ a robust estimator for wave overturning for both solitary and quasi-regular breaking waves in shallow water conditions. The newly presented method is verified in section 4.

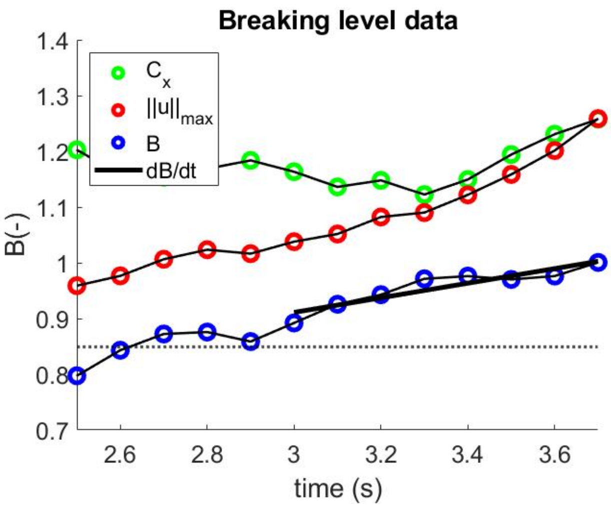

Figure 8: Breaking index as a function of time

4 Results undisturbed waves

After wave simulation in OceanWave3D, the simulation is redone in OpenFOAM without structure. This section describes the results from the undisturbed wave analysis in OceanWave3D and OpenFOAM and their differences. The breaking onset, incipient point and the moment prior to impingement are seen in Figure 9 at $2.9s$, $4.5s$ and $6.1s$.

Environmental conditions OCW3D

OceanWave3D has a numerical domain with a length of $1000m$. In the wave generation zone the water depth is $38m$. In the relaxation zone the water depth is $30m$. Between the locations $400m$ and $600m$ the water depth decreases with a ratio of $1 : 21$. A visualization is shown in Figure 2. OceanWave3D distributed its cells over the varying water depth. A total of 15 cells are chosen in vertical direction with more cells distributed at the free surface. The horizontal cells have a spacing of $1m$. The time step in Oceanwave3D is set at $0.1s$. The wave generation zone and relaxation zones have a length $200m$. A 3-hour-design-storm is simulated with a significant wave height of $10m$ and a peak period of $10s$ ($\lambda_p = 145m$). These parameters correspond to a 100-year storm, see Figure 10.

Grid specification VOF method

The OpenFOAM domain has a length of $300m$. The inlet is located at $100m$ before breaking onset as calculated in OceanWave3D. The inlet coupling zone is $50m$ and the outlet coupling zone is $30m$ Figure 2. The cells in OpenFoam have a cell size of $0.2m$ in x and z direction. The top 25% cells in the air phase and the bottom 12.5% cells are stretched in z-direction to reduce the number of cells. The middle of the domain near the free surface consists of square cells. The OpenFOAM bathymetry is made using the 'edges' command in the 'blockMesh' file to create an even cell size distribution. The time step is based on the Courant number and the output has a time interval equivalent to the OceanWave3D time step ($0.1s$).

4.1 Results Oceanwave3D

The approach (subsection 3.2) has detected a total of 343 breaking events occurring between $340m$ and $640m$, for waves with a minimum surface elevation of $5.5m$. The waves are selected for future analysis based on their maximum surface elevation

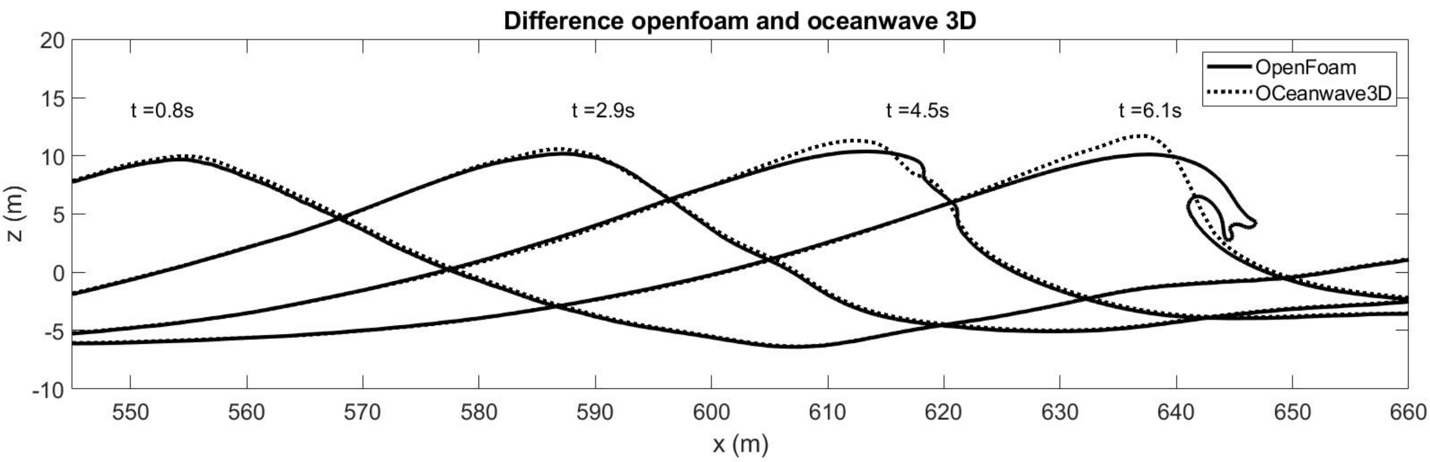

Figure 9: OceanWave3D and OpenFOAM free surface simulation Wave A

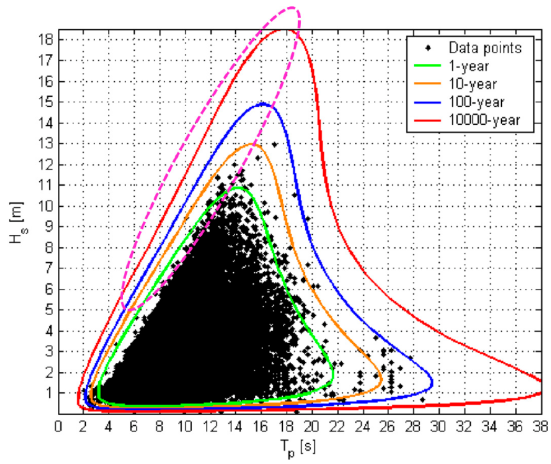

Figure 10: Environmental contour lines for the northern North Sea, including an indication of critical wave impact area (dashed pink) taken from Stansberg, 2020

and their breaking index. An overview of the selected waves is shown in Table 1, with letters further in the alphabet corresponding to increasingly smaller surface elevations. From Table 1 it is seen that breaking occurs independently of bottom geometry due to the effects of wave focusing (Bos and Wellens, 2021). This further emphasises the importance of the kinematic breaking criterion (Barthelemy et al., 2018). Additionally it is seen that the breaking index (Γ_{wave}) is unrelated to the maximum surface elevation (η) at breaking onset ($B = 0.85$). There is a slight correlation between the wave particle velocity and the maximum surface elevation at the moment of breaking onset - higher waves typically have higher particle velocities.

4.2 Results OpenFOAM

The OpenFoam results are divided into three subsets: (i) the relation between breaking onset and wave overturning, (ii) the relation between the breaking index and maximum occurring particle velocities and (iii) a clarification for the high particle velocities after breaking, for the wave with the highest particle velocities. From Table 2 the method of breaking identification in section 3 is verified, as the division of $|u|_m$ with C_x at the incipient point leads to a mean breaking criterion of 1.066 with a RMS error of 10.63%. Varing et al., 2021 found a value of 1.05

Table 1: Oceanwave3D data at B = 0.85

Wave	**x** (m)	η (m)	$\mathbf{C}_x$ (m/s)	$\|\|\mathbf{u}\|\|_m$ (m/s)	**dB/dt** (1/s)	Γ_{wave} (-)
A	582,16	10,29	11,15	9,55	0,11	0,83
B1	372,75	9,57	10,02	8,76	0,12	0,80
B2	470,94	9,36	10,37	8,90	0,12	0,80
B3	512,02	9,26	10,24	8,76	0,05	0,32
C1	600,00	8,89	10,19	8,74	0,01	0,30
C2	441,88	8,65	10,06	8,66	0,24	1,52
C3	353,71	8,64	9,60	8,38	0,58	3,60
C4	364,73	8,25	9,72	8,27	0,49	3,03
C5	348,70	8,09	9,24	7,99	0,33	1,96
D1	397,80	7,71	8,65	7,61	0,35	1,96
D2	549,10	7,43	8,81	7,79	0,53	2,99
D3	522,04	7,41	9,68	8,59	0,54	3,35
D4	455,91	7,06	8,79	7,71	0,52	2,94
D5	501,00	7,03	9,17	7,84	0,61	3,60
E	458,92	6,45	6,45	5,82	0,49	2,87
F1	372,75	5,97	8,21	7,21	0,58	3,07
F2	477,96	5,72	7,95	7,06	0,62	3,16

for solitary breakers with a RMS error of 3.2%. This difference may be due to the time step of $0.1s$, the tuning parameter in Equation 37 or the nature of irregular waves. This is a matter of further research.

Relation Breaking onset and incipient point

Table 2 shows significant differences between breaking onset and the incipient point. The breaking onset has a different location compared to the incipient point, there is a slight increase in surface elevation at the incipient point, there is a mean decrease in wave speed at the incipient point, while there is an increase in free surface particle velocity.

Difference in location breaking onset and incipient point
A relation for the location of breaking onset and the incipient point is investigated from the presented data in Table 2. The relation is shown in Figure 11. In Figure 11 a weak relation is seen between the location of the incipient point and the maximum surface elevation at breaking onset. There seems

Table 2: OpenFoam undisturbed wave Results

Wave	Breaking onset				Breaking index		Incipient point				max velocity	
	x (m)	η (m)	C_x (m/s)	$\|\|\mathbf{u}\|\|_m$ (m/s)	dB/dt (1/s)	Γ_{wave} (-)	x (m)	η (m)	C_x (m/s)	$\|\|\mathbf{u}\|\|_m$ (m/s)	$\|\|\mathbf{u}\|\|_m$ (m/s)	$\|\|\mathbf{u}\|\|_m^{nd}$ (-)
A	587.49	10.19	14.41	12.33	1.20	13.63	621.16	10.38	11.78	16.52	30.06	2.55
B1	382.64	9.34	14.74	9.34	0.85	8.70	385.27	9.39	12.69	13.03	25.56	2.01
B2	476.50	8.99	14.21	8.99	0.14	1.37	494.09	9.13	14.77	14.51	17.17	1.16
B3	461.00	9.60	9.88	9.94	0.12	0.73	485.00	9.20	14.22	14.43	19.78	1.39
C1	600.62	8.17	13.83	11.86	0.40	4.09	620.56	8.66	12.19	13.81	23.71	1.95
C2	443.11	8.00	13.08	11.13	0.37	3.21	453.44	8.28	12.75	13.65	17.29	1.36
C3	356.35	8.25	12.83	11.71	0.58	4.84	358.80	8.31	11.67	11.93	22.12	1.90
C4	365.35	7.36	10.92	11.06	0.90	6.29	370.15	7.58	11.60	11.99	23.39	2.02
C5	348.65	8.09	10.61	9.55	0.27	1.84	351.78	7.98	10.02	10.10	16.72	1.67
D1	396.56	7.36	11.17	10.09	1.41	10.17	397.56	7.38	10.08	10.46	20.09	1.99
D2	549.59	6.84	11.28	10.27	1.08	7.90	553.19	6.97	10.82	11.87	19.39	1.79
D3	523.18	6.76	12.87	11.12	0.64	5.48	524.40	6.80	11.12	12.22	21.71	1.95
D4	445.07	5.85	11.54	10.06	0.13	0.98	457.00	6.34	12.58	12.59	15.42	1.23
D5	499.27	6.46	6.46	8.79	1.13	6.39	500.20	6.50	9.36	9.23	18.48	1.98
E	460.29	5.54	11.20	10.68	1.05	7.55	460.31	5.54	11.20	10.68	18.07	1.61
F1	372.98	5.03	9.26	8.82	0.59	3.47	374.95	5.17	9.15	9.51	16.60	1.81
F2	466.77	5.18	11.46	10.18	0.49	3.60	480.25	5.34	8.97	11.68	17.17	1.91

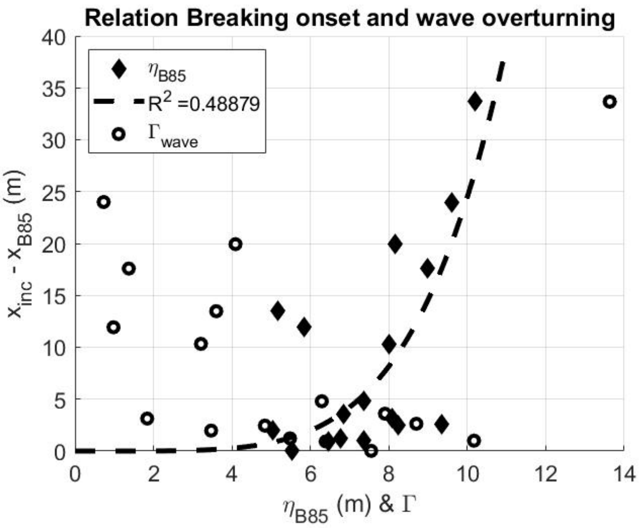

Figure 11: Relation breaking onset and wave overturning

to be no relation with the free surface particle velocity, wave speed and breaking index. It is seen that at breaking onset a wave may instantly overturn or at a distance of approximately $30m$ $(1/5\lambda_p)$.

surface elevation, wave speed and particle velocity

At the incipient point the surface elevation has increased on average with 1.7% with a RMS error of 2.7%. The wave speed decreases on average with 0.2% with a RMS error of 18%, this implies that a wave can endure acceleration or deceleration. It is estimated that strong plunging breakers have stronger wave speed deceleration, but this is a matter of further research. The free surface particles are accelerated with 18.2% compared to their breaking onset value with a RMS error of 17.2%, which implies the particles velocities are always higher at the incipient point compared to breaking onset. The exact mechanism leading to these values is a matter of further research.

Relation Breaking index and maximum particle velocity

An analysis is performed for the maximum occurring particle velocity after the incipient point and its relation with the breaking index. In Table 2 the breaking index, Γ_{wave} and the maximum non-dimensional free surface particle velocity, $||u||_m^{nd}$ are shown, determined according to

$$||u||_m^{nd} = \frac{max(||\mathbf{u}||_m|_{0<t<\infty})}{C_x|_{inc}}, \tag{40}$$

with $||\mathbf{u}||_m|_{0<t<\infty}$ the maximum free surface particle velocity and $C_x|_{inc}$ the wave velocity measured at the incipient point. The relation between the breaking index and the non-dimensional maximum free surface particle velocity is shown in Figure 12. In Figure 12 a relation is shown between the

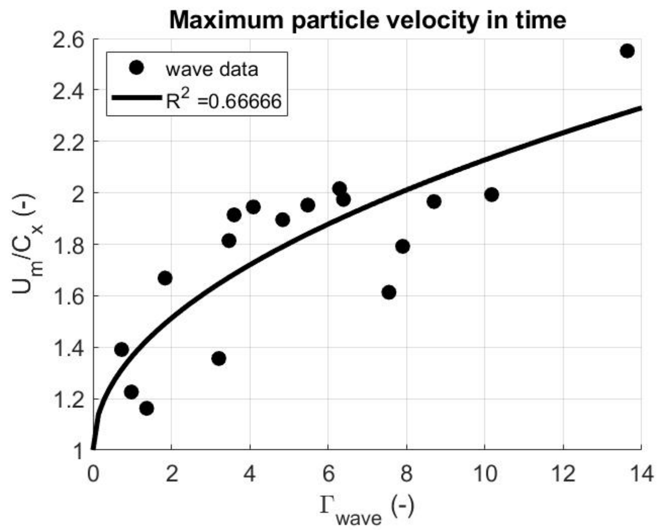

Figure 12: Maximum measured free surface velocity

breaking index and the maximum particle velocities. Generally waves with a high breaker index lead to high particle velocities. The relation between breaking index and non-dimensional particle velocities is approximated as

$$\frac{max(\mathbf{u}_m|_{0<t<\infty})}{C_x|_{inc}} = 1 + 0.365 \cdot \Gamma^{0.490}_{wave}. \tag{41}$$

Equation 41 has one as its minimum value, as the weakest spilling breaker has a breaking index close to zero, the RMS error is 33.3%.

Maximum particle velocity in space

Figure 13 displays the maximum occurring free surface particle velocity $||u||_m$ in space with the data sorted in time. In Figure 13 the maximum particle velocities occur after the incipient point, as zero in the horizontal axis corresponds to the point of overturning. It is seen that the maximum free surface particle velocities for this plunging breaker occur approximately $50m$ $(1/3\lambda_p)$ after the incipient point. It is also seen that this plunging breaker has a strongly decelerating wave speed before the moment of overturning. It is observed that the free surface particle velocities become more chaotic in time after reaching the maximum value of $30m/s$.

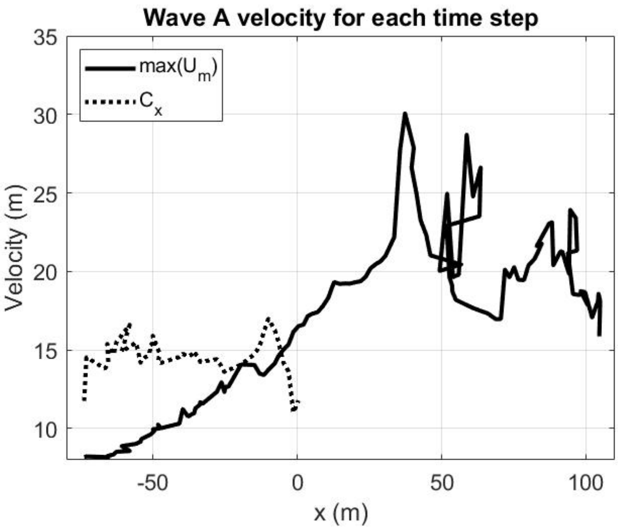

Figure 13: Free surface velocity wave A

Summarizing results breaking index relations

Summarizing, the breaking index can provide an estimate of the maximum particle velocities after the incipient point, based on data from before the moment of wave overturning.

Explanation high particle velocities after breaking

In Table 2 it is seen that wave A has the highest particle velocities, Here we will discuss the driving mechanism behind these large particle velocities. Table 3 and Figure 14 display the water particle velocities, $u \cdot \alpha$ at nine moments in time with keeping the x-axis fixed. Table 3 displays the corresponding maximum water particle velocities for each moment in time.

Analysis time panel 1 and 2

In Figure 14 at panel one and two, it is seen that the wave becomes steeper and that the particle velocities become larger. There is horizontal and vertical acceleration. The wave is not overturning, therefore there is no negative downward velocity $(-U_z)$. Breaking onset occurs somewhere between the second and third panel.

Analysis time panel 3

The incipient point is displayed at panel three. It is seen that the wave has a double vertical front. This implies the wave breaks due to the effects of wave focusing (Bos and Wellens, 2021), as two wave components break at the same time. This phenomena seems strange, but is a known occurrence among surfers, called the 'wave step' (SurferToday, 2019), which corresponds to the lower breaking wave as seen in Figure 15

Figure 15: Breaking wave at Shipstern Bluff, Tasmania, picture is taken with permission by Stuart Gibson

Analysis time panel 4

The moment prior to impingement is seen at panel four. In Table 3 a negative vertical wave velocity is observed, as the wave crest is about to hit the water surface. The horizontal particle velocities are still increasing. At panel four the upper part of the wave overtakes the wave step and forms a split jet prior to impingement.

Analysis time panel 5 and 6

After the impingement point, the water particles bounce off directed away from the water surface. This is due to the incompressibility of water. In Table 3 at panel five and six it is seen that there is a large vertical upward motion due to this particle bounce. The wave crest jet adds water particles to the bouncing particles, which consequently form a large detached body of water displayed at panel six. This body of water has relatively high velocity components.

Analysis time panel 6 and 7

Gravity pulls down the large body of water at panel six, which results in the large downward velocity seen at panel seven. Since the wave beneath the crest jet is moving forward, a surface slope is formed at panel seven.

Analysis time panel 7, 8 and 9

Gravity pulls down on the detached body of water at panel seven. As the large amount of water falls down it hits the surface slope. This results in a 'waterslide' mechanism. This 'waterslide' mechanism leads to high horizontal water particle velocities, as seen in panel eight. The high particle velocities at panel eight become more chaotic and swirls are formed. This results in velocity loss due to numerical dissipation and the formation of a new wave, birthed out of the breaking wave. Craciunescu and Christou, 2020 observed from their experiment a 20% energy loss of these newly formed waves compared to the wave before breaking. The exact (numerical) energy dissipation is not relevant for our consideration because in this study breaking waves interact with the structure after breaking.

Explanation high free surface particle velocities

This breaking mechanism is the driving factor for the high free surface particle velocities in focused plunging breakers.

Table 3: Wave A, maximum water particle velocities (m/s) at different time stamps and a fixed horizontal domain

U_x	9,8	12	16	18	24	22	22	34	23
$+U_z$	5,7	6,6	7,5	7,6	10	10	6,1	8,0	10
$-U_z$	0,0	0,0	0,0	9,3	12	6,6	8,4	10	7,3
U_m	9,9	12	17	20	26	23	22	34	23

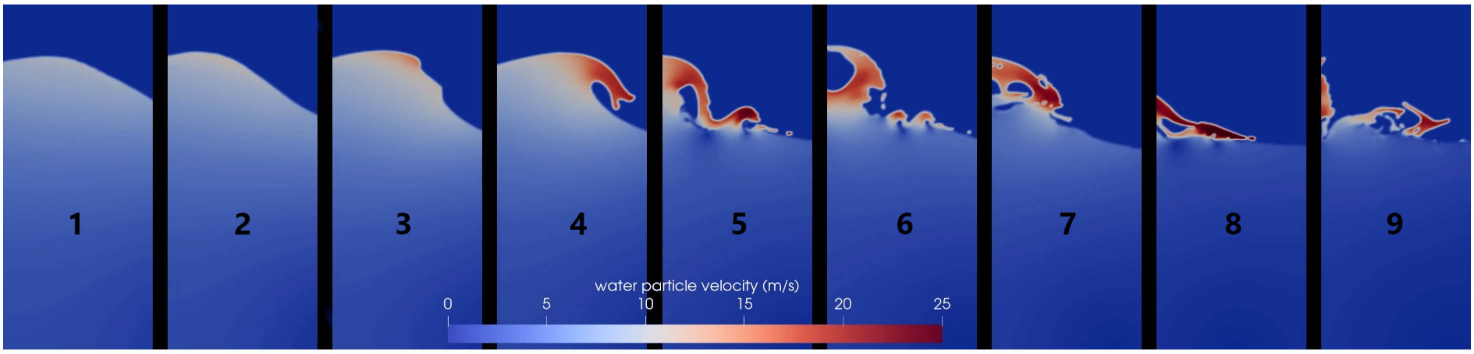

Figure 14: Wave A water particle velocities at different time stamps and a fixed horizontal domain

Multiple waves were analyzed and similar formations were seen for the plunging breakers B1, C1 and c4 (Table 2). A validation of this mechanism is a matter of further research.

Discussion OpenFoam results

From Figure 11 it is seen that an irregular wave may overturn between breaking onset and a distance of $1/5\lambda_p$. Between the point of breaking onset and the incipient point, the breaking index, Γ_{wave} is calculated. There is a relation between the breaking index and the maximum occurring particle velocities - The higher the breaking index the larger the particle velocities occurring in positive space and time direction. This effect is due to the incompressibility of water, which causes the impinging wave jet to detach off, away from the water surface. This water jet turns into a floating body of water. This body of water falls back on the water surface and leads to large horizontal velocity components. These large horizontal velocity components turn into swirls and form a newly shaped wave, birthed out of the focused plunging breaker. This setup has no turbulence, a cell size of $0.2m$ and no compression of air. Hence, physically after the impingement point, air is entrapped and eddies occur. These effects will results in energy dissipation. For the correct modeling of air entrapment and turbulence a finer mesh is needed.

4.3 Differences in methods OceanWave3D and OpenFOAM

The waves in OpenFOAM are coupled to OceanWave3D $3s$ $(3/10T_p)$ to $4s$ $(4/10T_p)$ before breaking onset is measured in OceanWave3D (Figure 9). This corresponds to the minimum time needed for the correct coupling of breaking waves. The presented method for wave speed calculation (subsection 3.3) is verified with the data presented in Varing et al., 2021. It is assumed that the OpenFOAM results are more valid compared to the OceanWave3D results for steep breaking waves so that the difference of OceanWave3D with OpenFOAM is considered an 'error'. An overview of the errors is shown in Table 4, with ψ a placeholder variable for the wave parameters calculated in OpenFOAM (OF) or in OceanWave3D (W3D). For each wave

Table 4: Difference OpenFoam and Oceanwave3D

	B = 0.85					
$\frac{\lvert\psi_{OF} - \psi_{W3D}\rvert}{\psi_{OF}}$	$\frac{\epsilon_\eta}{\eta}$	$\frac{\epsilon_{C_x}}{C_x}$	$\frac{\epsilon_{\lvert u\rvert_m}}{u_m}$	$\frac{\epsilon_x}{\lambda_p}$	$\frac{\epsilon_{dB/dt}}{dB/dt}$	$\frac{\epsilon_\Gamma}{\Gamma}$
$\overline{\epsilon}(\%)$	8,4	23.7	21.2	3.3	59.9	60.3
$\epsilon_{max}(\%)$	20.7	42.7	45.5	35.2	298.9	201.5

parameter the mean RMS error, $\overline{\epsilon}$ is given and the maximum RMS error, ϵ_{max}.

Difference in surface elevation

In Table 4 a mean RMS error of 8.4% is seen for the surface elevation at breaking onset. Figure 9 shows that OceanWave3D overpredicts the generated wave in OpenFOAM. To make a distinction between isosurface interpolating errors and mathematical solver differences, the surface elevation is compared for different breaking criterion values. The OceanWave3D surface elevation results are interpolated at the OpenFOAM surface elevation coordinates. The difference is taken for each coordinate and each time step up imtill the incipient point, which results in roughly 142.000 surface elevation data points. The results are shown in Figure 16. In Figure 16 the results are made non-dimensional by dividing by the peak surface elevation, η_{peak}, which is $5m$. It is seen that waves with gentle slopes ($B < 0.3$) have a mean error of 2.5%. This means the proposed method of isosurface interpolation leads to an error of $0.125m$. The error in surface elevation scales positively with the breaking criterion.

Difference in wave speed and particle velocity

In Table 4 a difference of 23.7% is seen for the wave speed, with a maximum RMS error of 42.7%. The free surface particle velocity has a mean RMS error of 21.2% and a maximum RMS error of 45.5%. This implies that OceanWave3D underestimates the wave speed and free surface particle velocities with approximately 22% compared to the OpenFOAM results at breaking onset.

Difference Breaking onset location

Table 4 states that the breaking onset location has a mean RMS error of 3.3%, which is significantly lower than the wave speed and particle velocity errors. This is unexpected as the

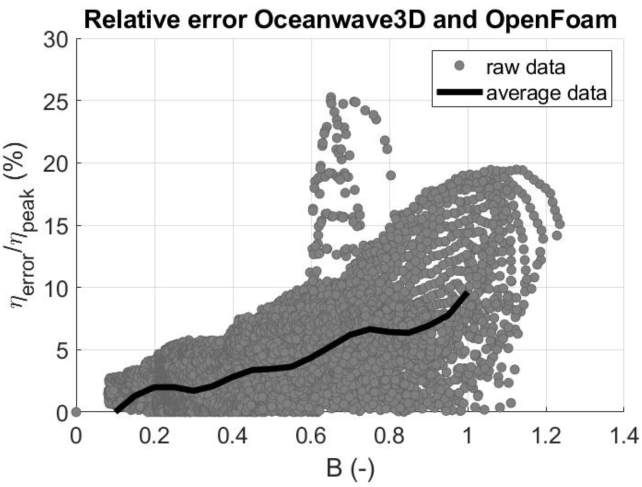

Figure 16: Difference Oceanwave OpenFoam wave A

breaking onset location is dependent on the wave speed and particle velocity (Equation 17). In Figure 17 the velocity errors are plotted for $max(B)$ at each time step up to the incipient point. From Figure 17 it is observed that the velocity errors

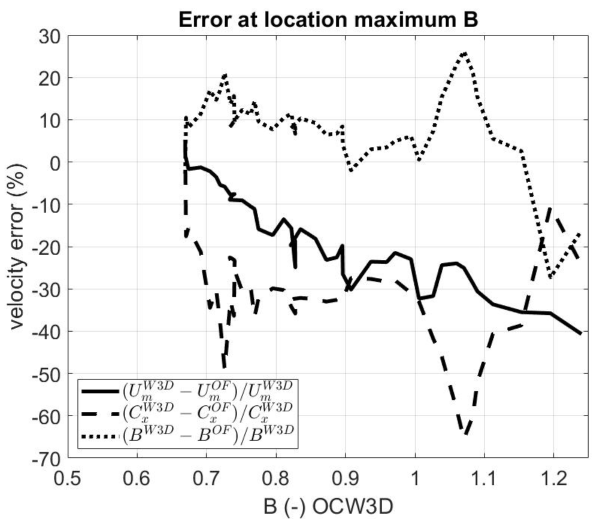

Figure 17: Difference numerical methods (wave A)

are proportional. Since the kinematic breaking criterion is calculated by the free surface particle velocity divided by the wave speed (Equation 17), the velocity differences cancel out. This explains the relatively low difference in B (Figure 17). The OpenFOAM-OceanWave3D breaking onset error range is approximately between $1/3\lambda_p$ and $1/15\lambda_p$, this implies that the breaking onset in OceanWave3D can occur at roughly $10m$ before breaking onset in OpenFOAM. Additionally, the breaking onset in OceanWave3D can occur around $50m$ after the breaking onset is measured in OpenFOAM. With this setup it is concluded that OceanWave3D is able to predict breaking onset comparatively well, due to the velocity errors being proportional.

Difference in breaking index

The breaking index error in Table 4 is 59.9% for the dimensional variant and 60.3% for the non-dimensional value. Therefore it is concluded that OceanWave3D is not able to predict the level of which a breaking wave undergoes plunging and its accompanied maximum particle velocities in a VOF-solver (OpenFOAM). However, OceanWave3D is able to determine if and where a wave will break.

Discussion differences OceanWave3D and OpenFOAM

OceanWave3D is a fast tool to make an estimation of the breaking onset location and the accompanied surface elevation. For this setup it was concluded that OceanWave3D is not able to determine the breaking index as it underestimates the wave velocities leading to a wrong breaking index. For breaking wave screening in OceanWave3D it is advised to re-simulate the undisturbed wave in a VOF-solver for breaking index and maximum particle velocity estimation. An OceanWave3D grid with a higher resolution may lead to less differences in wave speed, free surface particle velocities and breaking index calculation. A validation experiment is needed to determine the correct wave parameters and to make a grounded statement on the mathematical correctness of OceanWave3D and OpenFOAM for steep breaking waves.

5 Results waves and structure

This section describes the wave-induced loads and fluid-structure interaction with the sea wall and platform. The simulation setup and the calculation of the slamming loads is introduced in subsection 5.1. For each wave, the structure is placed at its incipient point to be able to compare wall velocity and loads (subsection 5.2 and subsection 5.3). Then for the three waves with the largest forces on the platform when positioned at the incipient point, the horizontal position of the wall is varied around the original position in order to investigate the effect of position on the maximum force on the platform. (subsection 5.4 and subsection 5.5). A sensitivy study is described in subsection 5.6. To conclude this section an analysis for wave screening in OceanWave3D is discussed in subsection 5.7.

5.1 Simulation setup with structure

theoretical simulation setup

The 3D monopile is approximated as a 2D Ꞁ-profile to find the fundamental mechanisms leading to vertical loads on the platform. Figure 18 gives a sketch of the 2D structure. The

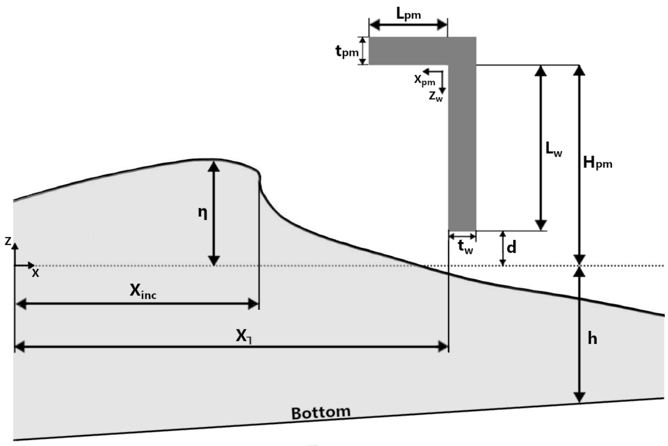

Figure 18: Sketch of the theoretical approach

structure has a wall length $L_w = 9.6m$. The sea wall has a thickness of $t_w = 1.6m$. its bottom is placed $d = 3.2m$ above mean sea level to prevent interaction with the waves preceding the breaking wave. The platform is placed at elevation $H_{pm} = 12.8m$ relative to mean sea level. The platform has a length

$L_{pm} = 4.6m$ with thickness $t_{pm} = 1.6m$. The structure is placed first at the incipient point x_{inc}. Then its position is varied with a distance $x_{\urcorner}$ relative to x_{inc}. The water depth h is a function of x and waves with surface elevation η are generated in the coupling zone (section 2). For presenting pressures and other output it is convenient to define an axis system (x_pm, z_w), with its origin where the largest pressure is expected.

Simulation setup OpenFoam

The cells of the structure are removed from the domain with the 'castellatedMesh' function. No snapping is used as this generates non-rectangular cells. Refinements zones were not used, as these influence the point of overturning (section 5.6). The mesh near the structure is shown in Figure 19.

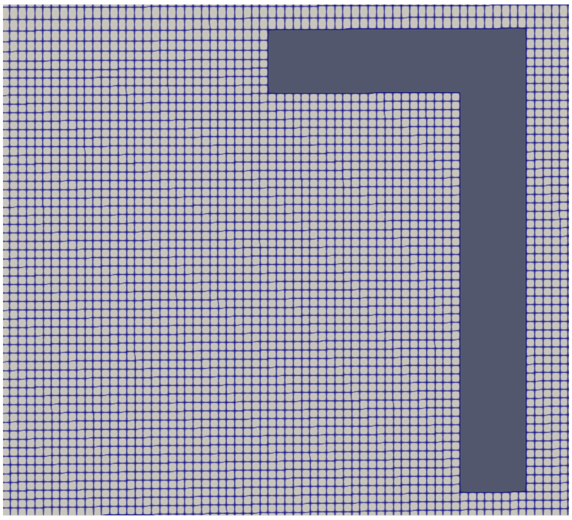

Figure 19: Grid around structure

Background information slamming

The wave impacts on the structure can be considered slamming, slamming is a complex phenomenon which was first analyzed by Von Karman, 1929 and improved by Wagner, 1932. A simplified second order slamming case of a parabolic shape of water hitting a flat plate was investigated by Korobkin, 2007, The wetted length was derived as

$$c(t) = 2\sqrt{t} + \mathcal{O}(t^{3/2}) \quad (t \to 0), \tag{42}$$

with t the impact time and c the wetted length. To estimate the pressure on the platform, the water velocity along the sea wall just before platform impact is needed, therefore a time derivative of Equation 42 is required. For our applications, it is nearly impossible to determine the platform loads analytically because the shape of the wave does not satisfy a function like Equation 42 that we can take the time derivative of. Our approach is to find the time dependent force by means of numerical simulation with OpenFOAM and integrating pressures along the contour of the platform

$$F_t = \int_0^{L_{pm}} p \, dx_c, \tag{43}$$

with p the time dependent pressure distribution on the platform, F_t the time dependent platform force and x_c the horizontal coordinate along the length of the platform (Figure 18). The maximum local pressure, force and moment are calculated with

$$P = \max(p), \tag{44}$$

$$F = \max(F_t), \tag{45}$$

$$M = \max(F_t \cdot x_F), \tag{46}$$

with x_F the centroid of the force integration along the platform. It was necessary to output the pressures at the cell faces (Figure 19) during run-time and post-process the integrals ourselves, instead of outputting the force directly, to get a correct slamming force estimate.

5.2 Wall velocities at the wave incipient point

It is challenging to obtain a fair comparison of the wave impact loads between different waves, because wave breaking is a highly chaotic phenomenon. The assumption is made that placing the structure at the incipient point of the breaking wave initially will allow us to compare the loads of different waves with each other. The assumption is tested by systematically varying the horizontal position of the structure for the three waves that yield the largest impact loads on the structure.

Relation free surface particles sea wall and platform

Before the wave hits the platform, it hits the vertical wall. We aim to analyse the relationship between the undisturbed wave velocities and the vertical run-up velocities along the vertical wall. The results in Table 2 show a weak relation of the undisturbed free surface particle velocity with the run-up velocity along the wall. The results are also shown in Figure 20. From the results in Figure 20, the following relation is obtained

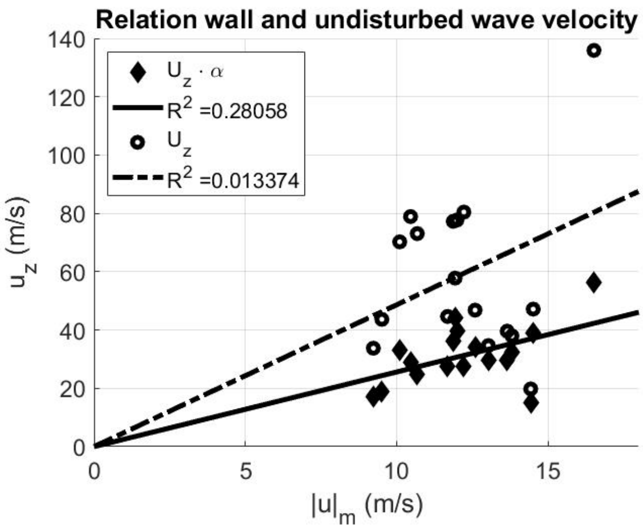

Figure 20: Relation undisturbed wave velocity and maximum run-up velocity along the wall at the incipient point

for estimating the vertical run-up velocity along the wall for given undisturbed free surface particle velocity

$$U_z \cdot \alpha = 2.56 \cdot ||u||_m, \tag{47}$$

with $U_z \cdot \alpha$ the vertical run-up velocity. The coefficient of determination equals $R^2 = 0.28$. This implies that in the interaction with the vertical wall the water particles are accelerated to a velocity approximately 2.5 times their undisturbed free surface

Table 5: Incipient point structure data for transposed coordinate system x_{pm} and z_{wall}, with $x_M = x_F atM$

Wave	Wall velocity		Maximum Loads			Centroids				Critical time stamps			
	$U_z \cdot \alpha$ (m/s)	U_z (m/s)	P (MPa)	F (N/m)	M (MN m/m)	$z_{Uz\cdot\alpha}$ (m/s)	z_{Uz} (m/s)	x_F (m)	x_M (m)	$t_{Uz\cdot\alpha}$ (s)	t_p (s)	t_F (s)	t_M (s)
A	56,20	135,89	2,15	1,11	1,78	2,59	7,21	0,33	2,00	0,20	0,24	0,24	0,47
B1	29,59	34,65	0,93	0,59	0,59	2,28	2,49	0,33	1,49	0,51	0,59	0,60	0,94
B2	38,87	47,16	1,22	0,30	0,10	2,24	3,05	0,17	0,82	0,55	0,61	0.617	0.967
B3	15,08	19,79	1,13	1,43	1,43	1,39	0,79	1,00	1,00	0,95	0,98	0,98	0,98
C1	32,41	37,97	1,20	0,44	0,12	2,32	4,29	0,21	0,30	0,44	0,52	0,52	0,53
C2	29,62	39,60	0,83	0,40	0,11	3,26	3,87	0,27	0,27	0,48	0,61	0,61	0,61
C3	44,11	57,80	0,91	0,21	0,12	4,97	5.39	0,10	0,97	0,20	0,34	0,34	0,88
C4	39,65	77,71	0,62	0,13	0,07	6,01	6,21	0,09	0,60	0,16	0,34	0,34	0,54
C5	33,24	70,23	0,43	0,06	0,02	6,36	6,75	0.37	0,37	0,15	0,38	0,58	0,58
D1	28,98	78,90	0,30	0,05	0,01	6,63	7,25	0,06	0,31	0,11	0,39	0,39	0,61
D2	36,31	77,28	0,43	0,09	0,02	6,54	7,29	0,08	0,38	0,10	0,33	0,33	0,49
D3	27,45	80,45	0,32	0,11	0,04	7,27	7,85	0,26	0,49	0,06	0,38	0,53	0,61
D4	34,09	46,82	0,41	0,07	0,02	6,09	6,30	0,07	0,83	0,18	0,40	0,41	0,61
D5	17,23	33,75	0,13	0,04	0,04	8,41	0,16	0,16	0,16	0,10	0,66	0,68	0,68
E	24,83	73,05	0,20	0,03	0,00	7,29	8,41	0,05	0,05	0,06	0,44	0,44	0,51
F1	18,73	43,66	0,00	0,03	0,00	7,66	8,29	0,04	0,13	0,06	0,59	0,59	0,61
F2	27,68	44,64	0,32	0,06	0,01	6,96	8,16	0,07	0,77	0,10	0,40	0,40	0,58

velocity. The low coefficient of determination may result from not including the shape of the wave in the analysis (Korobkin, 2007). The horizontal platform limits the development of the run-up, adding an additional level of complexity to the analysis. After impact with the horizontal platform, there does not seem to be a relation of the air and water velocities along the platform anymore.

Velocity distribution along the sea wall wave C3

In Figure 21 the total fluid and water particle velocities are shown for wave C3 at different moments in time. The velocities can be distinguished from each other by scaling them with volume fraction α. Wave C3 is selected from Table 5, because waves A and B features too many droplets for a consistent analysis. The time start when a value of $\alpha = 0.5$ is measured at any vertical location along the wall (note that $z_{wall} = 0$ is actually in the middle of the grid cell in the corner that connect to both the wall and the platform, so $0.1m$ away from where the wall and platform themselves meet, see Figure 21). The free surface configuration of the wave impact at $t = 0.098s$ with the wall forces air particles towards the platform with a high vertical velocity. The water particles reach their maximum velocity at 0.2s, $5m$ below the platform. The velocity distribution when the vertical impact force is at maximum at time $t = 0.335s$ is also shown. At that moment a droplet of water has disconnected from the main body of water and induces the maximum pressure load.

Location maximum velocity sea wall

The maximum velocity in either air or water occurs on average $6m$ below the platform with a RMS error of 38%. The maximum vertical water velocity along the wall is reached on average at $0.26s$ with a RMS error of 91.71%. Figure 22 shows the relation between the undisturbed maximum surface elevation of the wave and the vertical position of the maximum velocity along the wall. In Figure 22 the data approximately follow a linear relation between position of maximum velocity and location of maximum run-up velocity with a coefficient of 1, so that $z_{max(Uz)} = \eta$ with a R^2 value of 0.7068.

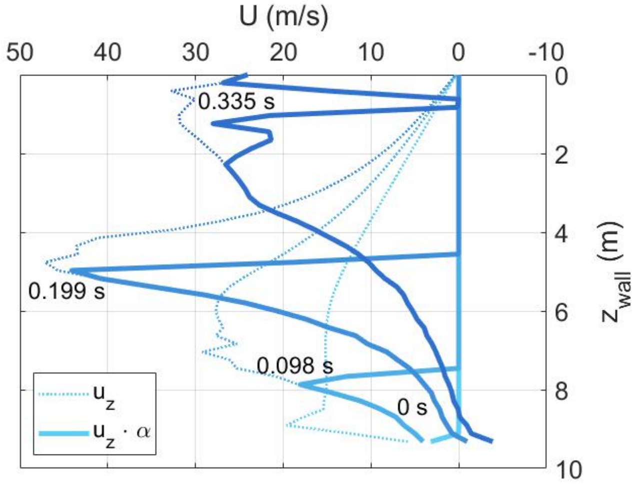

Figure 21: Vertical velocities along sea wall wave C3

Discussion wall velocity results

There is weak relation between the maximum measured wall velocity and the maximum undisturbed free surface velocity, while there is a strong relation between the location of maximum wall velocity and the maximum undisturbed surface elevation. The large scatter in the run-up velocity is likely caused by the shape of the wave impacting the structure (Korobkin, 2007), but also the presence of the horizontal platform. A multivariate analysis with the breaking index may lead to a better approximation of the maximum wall particle velocities. This is a matter of further research.

5.3 Loading at the wave's incipient point

In Table 5 the maximum loads are given together with the times that they occur (time again starts when a value $\alpha = 0.5$

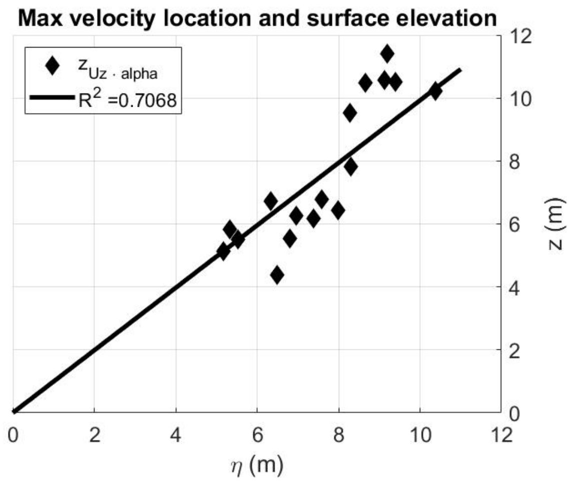

Figure 22: Relation undisturbed maximum surface elevation of the wave and the maximum run-up velocity location along the wall

is measured at any vertical location along the wall). In order of occurrence: (i) the maximum velocity along the wall at occurs on average at $t = 0.26s$ with a RMS error of 91.71%; (ii) the maximum local pressure is observed in the corner of the structure on average at $t = 0.48s$ with a RMS error of 36.07%, (iii) the maximum force on the platform takes place at $t = 0.50s$ with a RMS error of 34.05%, shortly after the maximum local pressure takes place, and (iv) the maximum overturning moment occurs at $0.66s$ with a RMS error of 25.2%, some time after the maximum force occurs. The signals of velocity, pressure, force and moment for wave A are shown in Figure 23 as a function of time.

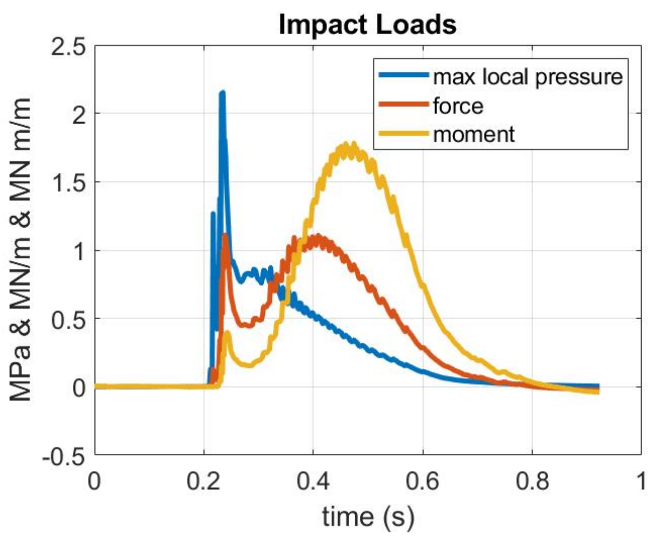

Figure 23: Time signals of vertical velocity along the wall, pressure in the corner, force and overturning moment on the platform for wave A

Explanation Maximum loading order

Figure 23 also shows the maxima of the signals and the time at which they occur. An explanation for the difference in times at which the maxima of the loads take place can be given in terms of the centroids of the integration of the pressure in space along the platform. In Figure 24 the spatial distribution of the pressure is visualized for the critical moments in time. First the water in the overturning jet protruding from the

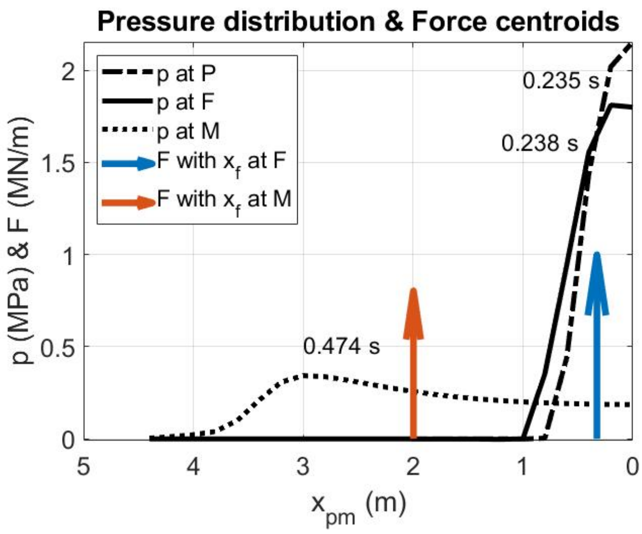

Figure 24: Pressure distributions wave A at critical moments in time

wave hits the wall, where some moments later the maximum vertical velocity along the wall takes place. The run-up propagates towards the platform, where, at the moment the run-up reaches the platform, the maximum pressure occurs. As the run-up transports more water towards the corner while the velocities and pressures are still fairly high, the maximum force on the platform takes place with a centroid of the pressure integration close to the origin of the platform. As more water accumulates in the corner of wall and platform, the velocities and pressures become lower, but the centroid of the pressure integration shifts to a distance further away from the origin of the platform. This mechanism leads to the occurrence of the maximum overturning moment.

Maximum local pressure analysis

In Figure 25, wave parameters η, the maximum free surface elevation, u_m, the maximum absolute particle velocity at the free surface and U_z, the maximum vertical run-up velocity, are plotted against the maximum pressure on the platform for those wave parameters. The relation with the wave speed is not displayed as it is approximately equal to the particle velocity at the incipient point (Varing et al., 2021). The breaking index is not displayed as the data near the incipient point is too scattered. From Figure 25 approximate relations are obtained for the maximum local pressure with the surface elevation, the free surface particle velocity and the wall run-up velocity. The pressure as a function of surface elevation relation then becomes

$$P_{inc} = 88.84 \cdot \eta_{inc}^{4.29}, \tag{48}$$

with P_{inc} the maximum local pressure (Pa). The surface elevation, η_{inc} is measured at the undisturbed wave's incipient point. The relation has a coefficient of determination of 0.90. The relation with the undisturbed particle velocity is

$$P_{inc} = 7.94 \cdot |u_m|_{inc}^{4.46}, \tag{49}$$

in which $|u_m|_{inc}$ represents the maximum free surface particle velocity at the incipient point. The accompanied coefficient of determination equals 0.89. The relation with the run-up velocity along the wall is

$$P_{inc} = 441.46 \cdot U_{z,inc}^{2.08}, \tag{50}$$

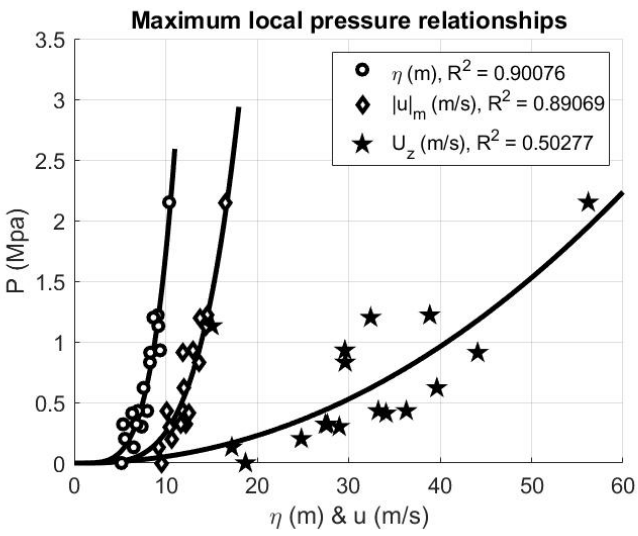

Figure 25: Relation wave parameters (maximum surface elevation η, maximum free surface particle velocity u_m and maximum run-up velocity U_z) versus local maximum pressure on the platform

with $U_{z,inc}$ the maximum run-up velocity. The relation between run-up velocity and pressure has a R^2 value of 0.50, which is lower than for the relation between undisturbed free surface particle velocity and pressure. This was contrary to expectations. The lower coefficient of determination could be due to the large scatter in Figure 20 for the relation between the free surface particle velocities and the maximum run-up velocity, but it is a matter of further investigation. There seems to be a weak relation with the wave speed as it has a coefficient of determination of 0.349 (not shown in figures). As mentioned, the breaking index data was too scattered and no relations were found.

Discussion wave parameters and platform pressure

From the results it is concluded that the wave surface elevation and the free surface particle velocities are a good screening parameters for determining the maximum local pressures on the platform, when the platform is placed at the incipient point. The run-up velocity has a weak relationship with the maximum local pressure and the wave speed has a weaker correlation compared to the free surface particle velocity. There is no relation with the breaking index. The weak relation with the run-up velocity raises questions on the relation between run-up and platform pressures. Additional research is needed for determining the relation between the maximum run-up velocity and the maximum local pressure, with and without a platform. Future run-up studies are advised to redo experiments without, but also with a platform present, as the largest run-up may not lead to the largest local pressure.

Maximum slamming force analysis

In Figure 27, wave parameters η, u_m and U_z are plotted against the force induces by the waves with these parameters. From the data in Figure 25, the relation between force and surface elevation could be approximated as

$$F_{inc} = 1.55 \cdot \eta_{inc}^{5.80}, \tag{51}$$

with F_{inc} the force on the platform in (N/m). The coefficient of determination is 0.66. The relation between force and undisturbed particle velocity is

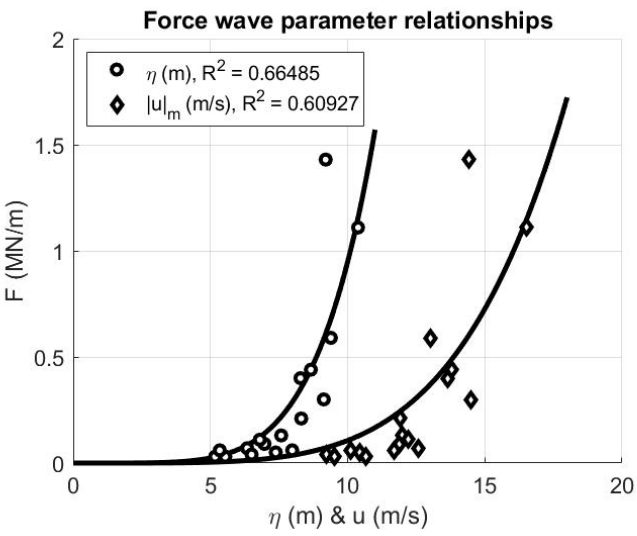

Figure 26: Relation wave parameters and platform force

$$F_{inc} = 0.26 \cdot |u_m|_{inc}^{5.49}, \tag{52}$$

The coefficient of determination for this relation is 0.61. The maximum force on the structure could not be related to the run-up velocity and no relation could be found between force and wave speed or breaking index.

The coefficients of determination for the relations between force and wave parameters are lower than those for the pressure and the wave parameters, which likely means that an important parameter is missing from this analysis. Using the free surface elevation gives the most reliable estimate of the platform force, while the reliability of using the free surface particle velocity is only fair.

Maximum overturning moment analysis

In Figure 25 the wave parameters η, u_m and U_z are plotted against the overturning moment induced by the wave. The

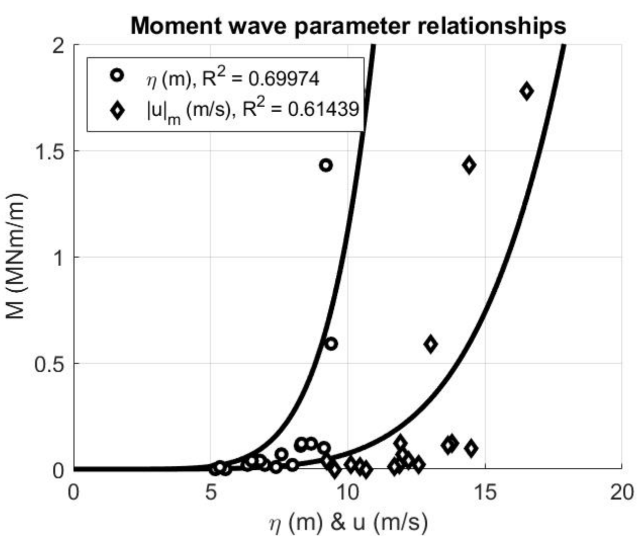

Figure 27: Relation wave parameters and maximum platform moment

relation between overturning moment and surface elevation is approximated as

$$M_{inc} = 1.55 \cdot \eta_{inc}^{5.81}, \tag{53}$$

with M_{inc} the overturning moment in (MNm/m). The coefficient of determination is 0.70. The relation with the undisturbed particle velocity is estimated as

$$M_{inc} = 0.26 \cdot |u_m|_{inc}^{5.49}, \tag{54}$$

with a coefficient of determination of 0.61. The coefficients of determination for the overturning moment are similar to those of the force. This is not unexpected as the equation for the force, (Equation 45), is similar to Equation 46

Discussion wave parameters and overturning moment on platform

From the analysis with the wave parameters it is concluded that the surface elevation is the best screening parameter for the maximum moment at the wave's incipient point. The free surface particle velocity gives a relatively good relation. There is no relation with the wave speed, breaking index and particle velocities along the wall. It is unknown if the platform endures more structural stress due to the local pressure force or moment.

Discussion results incipient point loading

The wave surface elevation and maximum free surface particle velocity are considered to be good screening parameters for estimating the wave impact loads with the platform at the incipient point. The wave speed and the breaking index can not be used for determining the maximum loads. The correlation between the maximum run-up velocity and the platform loads was considered to be insufficient. Multivariate analysis could lead to better wave parameter relationships. In future run-up studies it is advised to investigate the run-up thickness in combination with the run-up height, with and without the presence of a platform.

5.4 Loading for various platform locations

It can be concluded from subsection 5.3 that the waves with the highest particle velocities and largest surface elevation lead to the largest loads on the platform when placed at the incipient point. To investigate the sensitivity of the load for the position of the platform with respect to wave's position of breaking Bos and Wellens, 2021, wave A, B2 and B3 are selected to determine the effects of varying the horizontal position of platform and wall on the maximum loads. The platform is placed at 38 different locations for Wave A, 37 different locations for wave B2 and 31 different locations for wave B3. The approach is done in two steps. In the first step, the structure is shifted in horizontal direction from its original position at the incipient point with intervals of $5m$ between the position $1/3\lambda_p$ in front of where the breaking wave overturns and $2/3\lambda_p$ behind that position. In the second step, the resolution is increased near where the loads are at maximum with intervals of $1m$.

Highest loads are observed for wave A

It can be found from Table 6 that wave 'A' leads to the highest loads compared to wave B2 and B3. Figure 28 depicts the fluid structure interaction for wave A at nine different platform positions. The maximum loads occur if the structure is placed at $x_{\top} = 685m$, $64m$ after the wave's incipient point. The second highest load for wave A occurred at a platform location of $x_{\top} = 665m$, $44m$ after the incipient point. The highest load for a platform position before the incipient point was observed at $x_{\top} = 614m$, $7.2m$ before the incipient point (not displayed in (Figure 28). The loads follow a similar pattern in time as was described in subsection 5.3, with the maximum run-up velocity occurring first, followed by the maximum local pressure on the platform. Then the maximum force on the platform takes place, just before the maximum moment.

Pressure platform location analysis

In Figure 29 the maximum local pressures are displayed for various platform locations. The maximum pressures that occur for waves A, B2 and B3 are compared. InFigure 29 the maximum pressure for wave A occurs with the platform $64m$ behind the incipient point. The highest pressure with the platform before the incipient point occurs at $-8.2m$. For wave B2 the highest pressure is obtained with the platform at $40.91m$. With wave B2, the platform could not be shifted to all intended positions, because otherwise a preceding wave would interact with the structure and our intention was to consider the loads in single waves only. The highest pressure for wave B2 was measured for a platform position $5.1m$ before the incipient point. For wave B3 a single pressure peak was observed with the platform at a position $15m$ before the incipient point.

Explanation why wave A has the highest pressure

There are multiple maxima in the lines that connect the maxima of pressure on the platform as a function of the horizontal position of the platform. The second maximum of maximum pressure is explained by means of the breaking index. From Figure 12 and Figure 13 it is observed that the breaking index and the maximum particle velocities are related - the higher the breaking index, the larger the particle velocities after wave overturning. Higher particle velocities in a wave lead to higher pressures on a rigid object. Wave A has the highest breaking index of the wave considered leading to the largest pressure peak at $64m$. Wave B2 is a weaker plunging breaker, with a lower breaking index, which leads to a second pressure maximum equally large as the pressure maximum before the incipient point. Wave B3 does not have a second maximum of maximum pressure due to the low breaking index.

Force platform location analysis

In Figure 30 the maximum force on the platform in waves A, B2 and B3 is displayed for varying horizontal positions of the platform. In Figure 29 three maxima of the maximum force are observed for wave A. The first maximum occurs for a platform position $8.2m$ before the incipient point, the second maximum $43.8m$ after the incipient point. The third and highest force maximum occurs with the platform positioned $64m$ after wave overturning. Wave B2 has two maxima of maximum force. The first maximum occurs when the platform is at a position $6.09m$ before the incipient point, while the second maximum is obtained $40.9m$ after the incipient point. Wave B3 has a single maximum of maximum force on the platform with a platform placement of $10m$ behind the incipient point.

Explanation why wave A causes the highest Force

Wave A, B2 and B3 have a similar force maximum around $-8m$, which is highest for wave A. The first maximum compares

Table 6: Wave A: loads on the platform for different horizontal positions of the platform

$x_{\urcorner}$	570	590	605	625	645	665	685	700	715	m
U_z	17.64	23.44	32.17	69.19	55.24	35.33	96.13	50.21	26.45	m/s
P	0.51	0.77	1.54	2.56	3.40	2.12	4.43	2.77	1.13	MPa
F	0.44	0.68	0.93	1.15	1.35	3.93	7.12	2.37	1.34	$MN\frac{1}{m}$
M	0.66	1.17	1.41	1.88	2.05	3.84	14.63	1.52	0.97	$MN\frac{m}{m}$
x_F	1.21	1.19	1.21	1.28	0.28	0.98	2.05	0.64	0.63	m
x_M	1.73	1.83	2.00	1.91	2.10	0.98	2.05	0.64	0.93	m
$t_{Uz\cdot\alpha}$	0.62	0.54	0.45	0.13	0.17	7.64	0.27	0.30	0.75	s
t_p	0.69	0.56	0.46	0.16	0.21	7.71	0.30	0.32	1.11	s
t_F	0.92	0.77	0.64	0.33	0.22	7.71	0.38	0.33	1.11	s
t_M	1.02	0.85	0.73	0.39	0.52	7.71	0.38	0.33	1.12	s

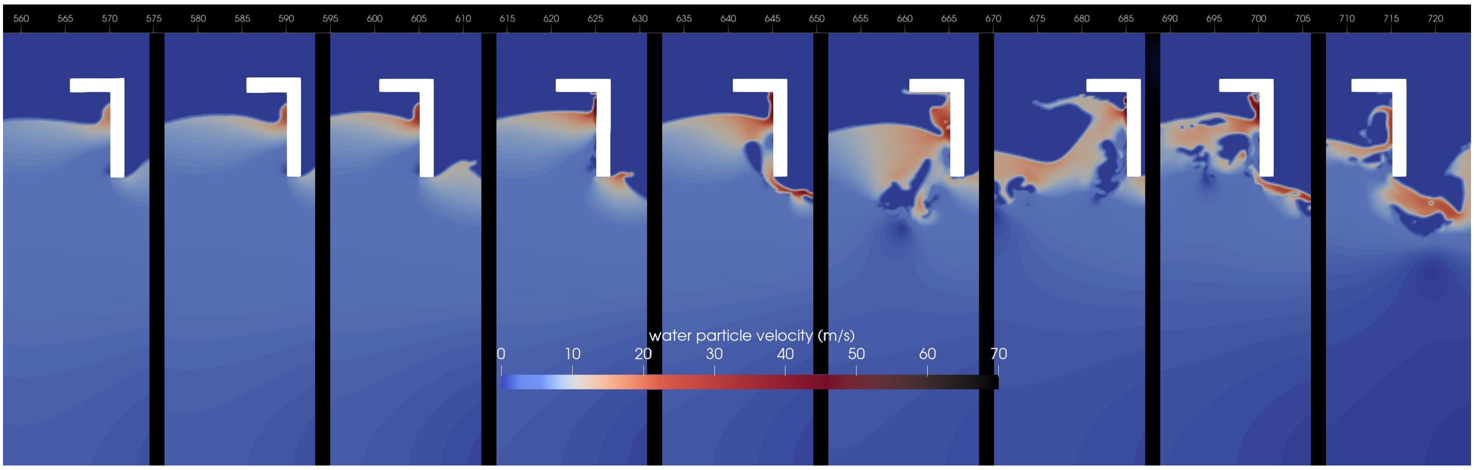

Figure 28: Wave A: pressure distributions in the water for various horizontal positions of the platform

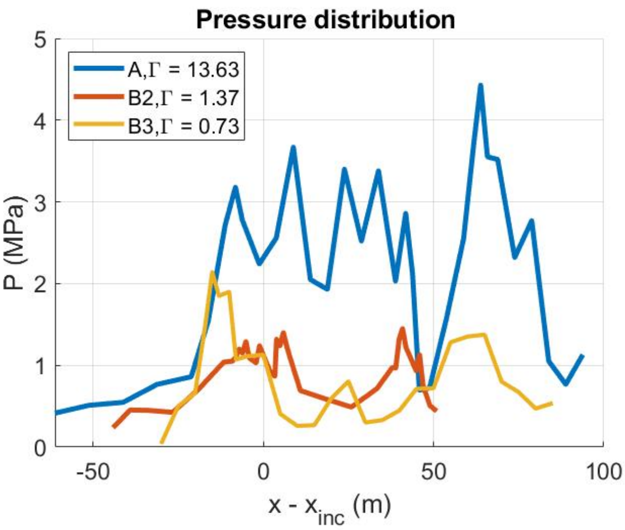

Figure 29: Comparison of maximum pressure on the platform in wave A, B2 and B3 for varying horizontal position of the platform

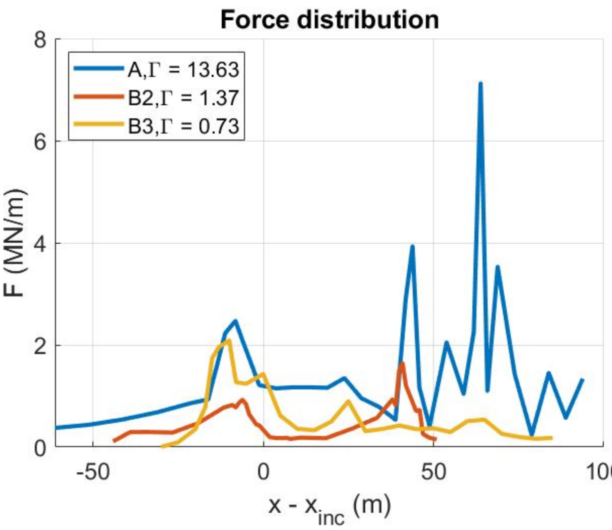

Figure 30: Comparison of maximum force on platform in waves A, B2 and B3 for varying horizontal platform positions

well with the results of Grue and Osyka, 2021, who observed that the highest run-up was achieved for a wave breaking violently just behind a monopile. The second and third maxima can be explained with the breaking index, just as the maximum pressures on the platform. Wave A and B2 have a second maximum in forces for a platform located approximately $42m$ after the incipient point. The fluid structure interaction for the second maximum of maximum force on the platform for wave 'A' is in panel six (from the left) of Table 6. That panel shows a comparatively thick run-up tongue directed towards the platform. For that same simulation, Table 6 reports a relatively low run-up velocity, wheres the largest run-up velocity in the table does not lead to the highest force. This is an indication of the importance of the thickness of the run-up tongue for the force on the platform.

Relation loads and undisturbed free surface velocity

subsection 5.3 described the relation between the free surface particle velocities and the hydrodynamic loads. That relation is now investigated for waves A, B2 and B3. The parameters are made non-dimensional by dividing them with values of the parameters at the incipient point.

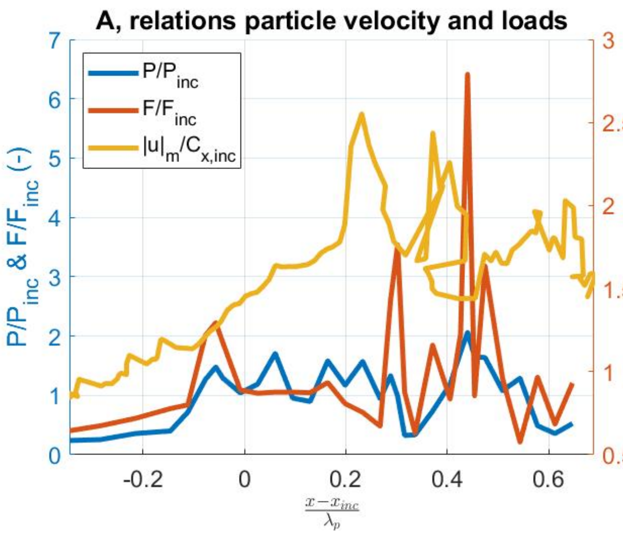

Figure 31: Relation maximum free surface particle velocity and loads wave A

Loads and particle velocity relation wave A

Figure 31 shows the relation for the maximum free surface particle velocity $|\mathbf{u}|_m$, the maximum local pressure P and the maximum platform force F for wave A. A pattern is observed: two maxima are observed for the maximum free surface particle velocity, corresponding to the second and third maximum in forces, with a phase shift of $10m$. No direct relation is found between the forces and the maximum free surface particle velocities with the platform just before the incipient point.

Observation largest loads before incipient point

The maximum forces with a platform placement before the incipient point of the breaking wave is found at $614m$. This corresponds to a value of approximately $1/20\lambda_p$ before wave overturning. At this platform a maximum pressure of $3.43MPa$ is obtained, and a maximum force of $2.28MN/m$. The centroid of the pressure integral along the platform is located at $0.39m$. The aforementioned maxima are all obtained for wave A. The reason why the maximum of the force with a platform position before the incipient point is obtained for specifically that platform position cannot be related to the magnitude of the free surface particle velocities alone. The reason becomes more clear if the force maximum is explained also with the direction of the free surface particles at the free surface, see Figure 32.

Observation particle velocities at first loads peak

In Figure 32 the undisturbed wave is depicted for three platform locations, $605m$, $614m$ and the incipient point $621.4m$, before the impact with wall and platform take place. The figure shows the position of the free surface together with the direction of the free surface particles velocities. The blue arrows represent the free surface particle velocities at the moment before impact with platform and wall placed at the incipient point. The purple arrows correspond the free surface particle velocities at the moment before impact with the structure

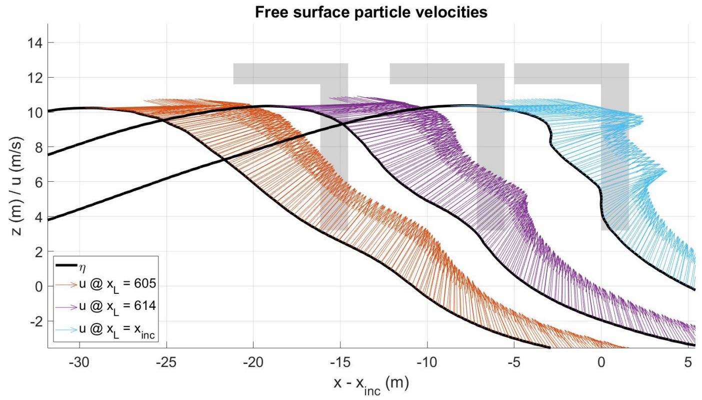

Figure 32: Undisturbed free surface particle velocities for wave A at three platform locations

placed $7.4m$ before the incipient point (the force peak as seen in Figure 31), the red arrows correspond to a platform placement $16.4m$ before the incipient point.

Explanation loads peak

The free surface configuration and free surface particle velocities for the platform position that leads to the largest force on the platform is depicted in Figure 31 with purple arrows. Apparently, when the free surface velocity is directed towards the corner between wall and platform just before impact (purple arrows), it lead to a larger maximum force than when the free surface velocity direction is more vertical (red arrows), or more horizontal (blue arrows).

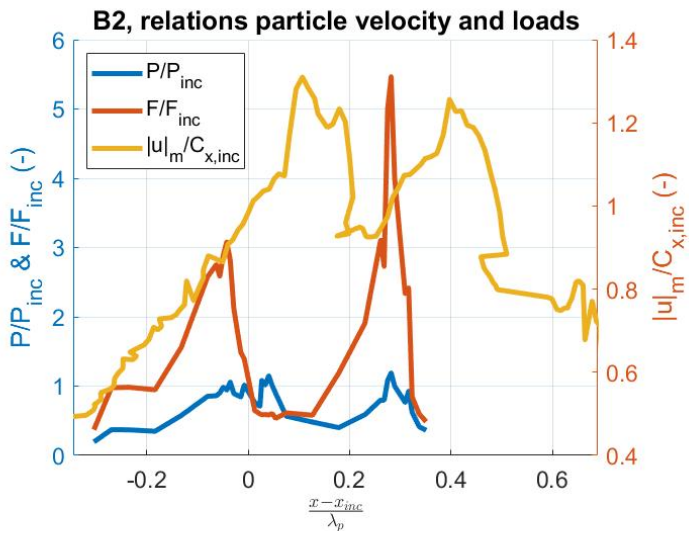

Figure 33: Undisturbed free surface particle velocities for wave B2 at three platform locations

Loads and particle velocity relation wave B2

From Figure 33 a similar pattern for wave B2 is observed as for wave A. It was not possible to find a third maximum in the representation of the force on the platform as a function of it position, because at the platform positions needed for that the wall started interfering with preceding waves. For wave B2 similar loads as function of position are seen before the incipient point as for wave A, with a maximum force measured for a platform located $6.1m$ before that point.

Loads and particle velocity relation wave B3

Wave B3 has no second maximum in the relation between force and platform position, see Figure 34. The likely explana-

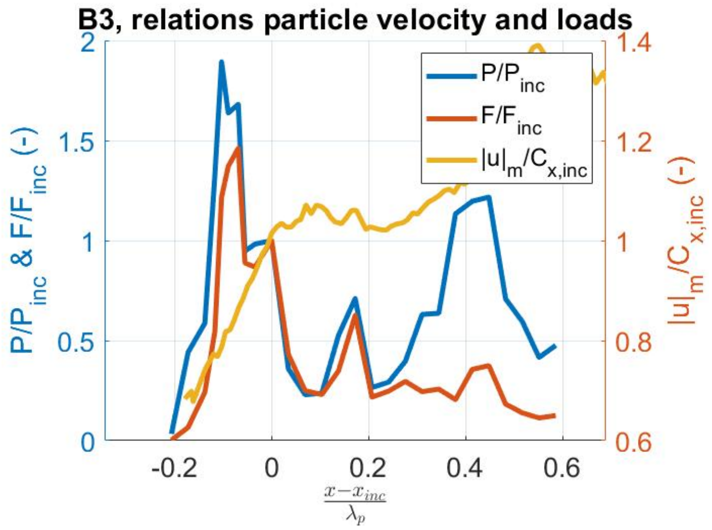

Figure 34: Relation maximum free surface particle velocity and loads wave B3

tion is that the maximum free surface particle velocity stays constant after the incipient point. After $50m$ from the incipient point of the wave, the free surface particle velocities increase due to the chaotic wave breaking effects. This has no effect on the structure due to the low breaking index. Wave B3 is a breaking wave with low breaking index, but a breaking wave nonetheless so that there is a force maximum at the same platform position as for wave A, before the incipient point.

Discussion loads for various platform locations

From the results it is concluded that the wave with the highest breaking index and the highest surface elevation, overturning approximately $4/9\lambda_p$ before the structure, induces the largest force on the platform. The maximum force is approximately 6.5 times larger than the force with platform placement at the incipient (Figure 31). The second largest force on the structure is estimated with a structure placement of $3/10\lambda_p$ after the incipient point.

A force maximum is observed for all breaking waves with a platform placement $1/15\lambda_p$ before the incipient point. This corresponds to the observations made by Grue and Osyka, 2021. This force has a value ranging between 1.5 and 3 times it's incipient point force. The force maximum occurs for a specific configuration of free surface and platform position, in which the free surface elevation and both magnitude and direction of the free surface velocity are thought to be the most relevant parameters.

In our approach the effects of turbulence, mixing of air and water, air compression and 3D effects are neglected. These effects may result in lower loads. However, it is estimated that the loads after the incipient point remain significant, as a second peak in energy transfer was also observed for aerated breaking wave impacts with a cylinder Bos and Wellens, 2021. The low energy loss for aerated wave impacts could be explained with the results from Craciunescu and Christou, 2020. Craciunescu and Christou, 2020 observed an energy loss of only 20% after breaking for focused breaking waves.

5.5 Free surface configuration and distribution of pressure during impact

The intention now is to zoom in to the moment of the impact of wave A and to study the pressure distribution in detail. Figure 35 shows the free surface configuration and the pressure distribution in the corner between platform and wall for three key moments: when the run-up velocity is at maximum, the pressure is at maximum and when the force is at maximum (which is almost equal to when the overturning moment is at maximum).

Free surface and pressure at time of maximum run-up velocity

In Figure 35 at time $0.274s$ after the moment the first occurrence $\alpha = 0.5$ is registered near wall and platform, the fluid configuration and pressure distribution are shown in the two graphs on the left at the moment the maximum wall velocity occurs. The figure is zoomed in with respect to panel 7 (from the left) in Figure 14. Close examination of the graph on the left of Figure 35 at time stamp $0.274s$ reveals a small jet forming directed towards the platform, with a maximum velocity along the wall of $96.13m/s$

Free surface and pressure at time of maximum local pressure

At time $0.301s$ the maximum local pressure is reached. This is shown in the two graphs in the middle of Figure 35 as a dark red area in the corner between platform and wall. This pressure zone in the corner of the structure generates fluid flow in negative x-direction along the bottom of the platform.

Free surface and pressure at time of maximum force.

The maximum force and overturning moment occur (nearly) simultaneously at time $0.378s$. In the graphs on the right of Figure 35 a zone with higher pressures is observed both water and air. The water encloses an air pocket. Because of the assumption of incompressibility of the air, the pressure in the air becomes equal to the pressure in the surrounding water the moment the air pocket is formed. This is likely different from what happens in reality.

Discussion

The configuration of the fluid and the pressures at key moments during the impact are discussed. Evolution of the free surface and pressure with the jets forming near the corner between platform and wall could resemble what happens in surf waves when they break and is called wave 'spit' (Howlermagazine, 2018). During surfing it can launch a surfer into the air; in the confined space near platform and wall it leads to high pressures and large forces. In a physical environment three dimensions are present, which would cause air pockets to be formed differently – if formed at all – and cause jets to be directed in y-direction. It is our impression that without air pockets the forces will not be much different from what is simulated here.

5.6 Sensitivity study

The sensitivity of the results, in terms of maximum force mainly, to changes in configuration of the domain has been investigated. The variation involve the configuration of the coupling zones and the cell size in OpenFOAM. The size of the coupling zones is varied as well as the position of inlet (end of inlet coupling zone) and position of outlet (start of outlet coupling zone) relative to $x_\top$. With the selected coupling zone dimensions,

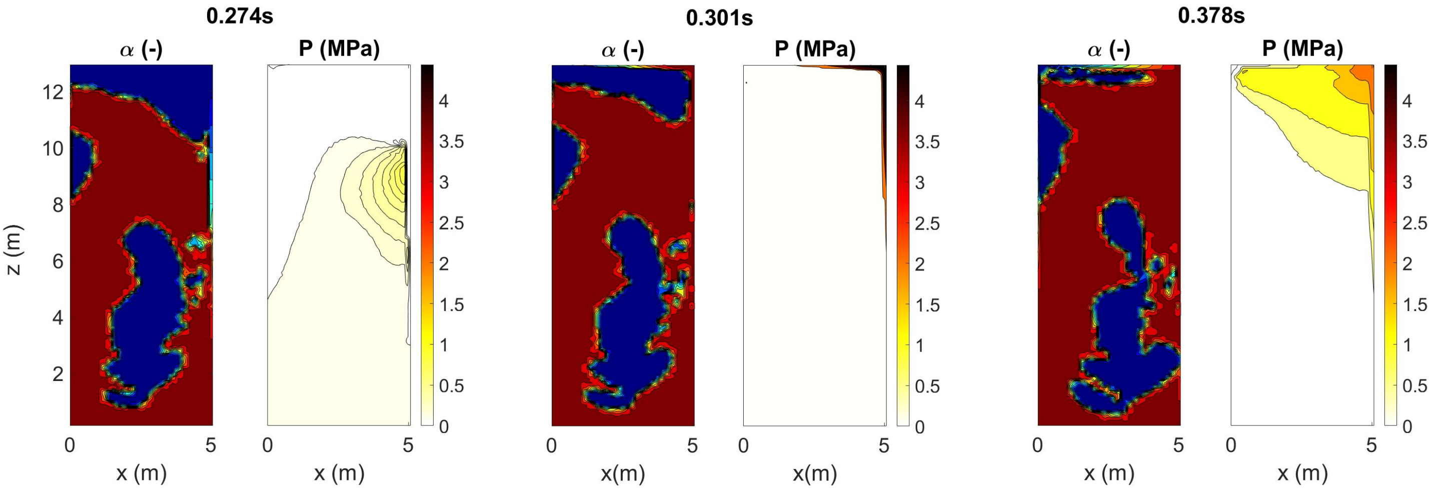

Figure 35: Detailed fluid configuration and pressure for wave A at $x_{\text{T}} = 685$, for the moments of maximum run-up velocity, maximum pressure and maximum force

then, a grid sensitivity study is performed. The sensitivity study is done for wave B2 with the position of the platform at $x_{\text{T}} = 502m$.

Outlet coupling zone sensitivity

A total of 24 variations were chosen for the outlet coupling zone, with the coupling zone size ranging from $10m$ to $200m$. No convergence was found. The standard deviation for the pressure was equal to 8.6%, with a maximum observed error of 22.0%. The standard deviation for the force was equal to 0.94%. Although no convergence was found, it was concluded that a relatively small outlet coupling zone can be chosen with an outlet position close to the structure without increasing the error in force. An outlet coupling zone size of $30m$ $(1/5\lambda_p)$ was chosen, with a minimum distance between the structure and position of the outlet of $10m$ $(1/15\lambda_p)$.

Inlet coupling zone sensitivity

A total of 21 variations were examined for the inlet coupling zone. The size of the coupling zone was varied between $10m$ and $450m$. No formal convergence was found for the inlet zone either. The standard deviation for the platform pressure was found to be 10.69% and the standard deviation for the platform force was estimated at 10.04%. A maximum pressure error was observed for 23.60% and a maximum force error was measured to be 43.90%. Based on the variations with the inlet coupling zone, a size of $50m$ $(1/3\lambda_p)$ was chosen, with a minimum distance of $50m$ $(1/3\lambda_p)$ between inlet and position of the structure. For this configuration of the inlet the error in the maximum force was not larger than 5% compared to a much longer coupling zone size.

Grid sensitivity study

A grid sensitivity study was performed in which the sensitivity was investigated of the position of the incipient point, the maximum local pressure on the platform and the maximum force. The analysis makes use of the method of Eça L., 2014.

From Figure 36 we find that no formal grid convergence is found for the position of the incipient point. A finer mesh leads to wave overturning closer to the inlet (Figure 2). This is in conflict with the observations made by Bredmose and Jacobsen, 2011. There, the incipient point shifted further downstream for for a finer mesh. The reason why our simulation results are different from earlier work is not yet understood.

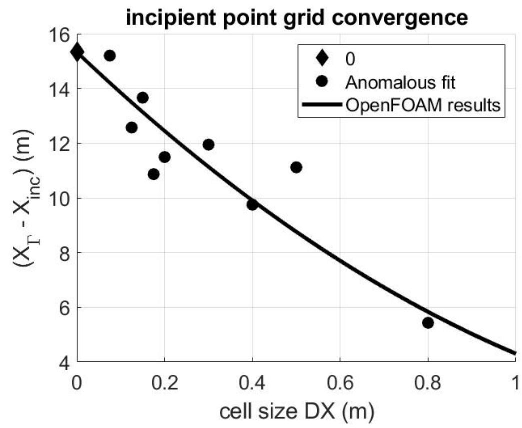

Figure 36: Incipient point relative to position of platform and wall for different grid sizes.

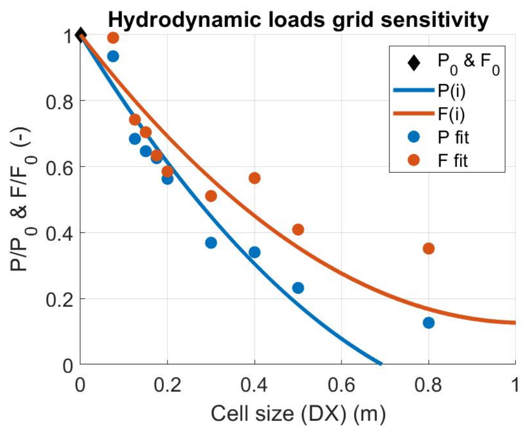

Figure 37: Maximum loads sensitivity study, data is made non dimensional with method described by Eça L., 2014

From Figure 37 no grid convergence is found either for the maximum local pressure and force. No grid convergence for the maximum loads is partly caused by the position of the incipient point, which has an effect on the loads (subsection 5.4. OpenFOAM is a low order method therefore finer meshes have lower numerical dissipation. This could lead to higher velocities and therefore higher loads. Another reason for the lack of grid convergence on the loads, is the short time duration of slamming. The pressure and force peaks as seen in Figure 23 happen at a small time scale. Finer meshes have a smaller time step due to the Courant number. The load maxima shown in Figure 23 could be missed with larger time steps. A final reason for the lack of convergence could be that wave breaking is a chaotic process. The choice is made to perform all simulations with a cell size of $0.2m$ as a compromise between accuracy and time required for the simulations. Validation with experiments is required to determine and adequate grid size.

5.7 Critical wave selection process

The objective of this paper is to find which wave selected from a sea state leads to the largest hydrodynamic loads on a monopile inspection platform. From subsection 5.4 a procedure for wave selection can be derived. That procedure is elaborated upon here.

OpenFOAM critical wave selection

In subsection 5.4, the maximum force on the platform was measured with the platform position at a distance of $4/9\lambda_p$ relative to the wave breaking point for a plunging breaker with a high breaking index. The first maximum force for all breaking waves is measured with the platform positioned at $1/15\lambda_p$ before wave overturning. This leads to the following range for critical wave selection

$$F_{\text{T}} = max \quad at \begin{cases} -\dfrac{1}{3}\lambda_p + x_{inc} < x_{\text{T}}, & max(\eta_{inc}) \\ \dfrac{2}{3}\lambda_p + x_{inc} > x_{\text{T}}, & max(\eta_{inc}) \cup max(\Gamma) \end{cases}, \tag{55}$$

with F_{T} the maximum force on the platform, λ_p the peak wave length, x_{inc} the location of wave overturning and x_{T} the structure placement. The waves with the highest surface elevation measured at the incipient point in the set of breaking waves is represented as $max(\eta_{inc})$. The waves with the highest breaking index from the set of breaking waves is represented as $max(\Gamma)$. The union of the two wave sets uses the symbol $\cup$. In horizontal space, it is not necessary to look for waves with an incipient point further than $-1/3\lambda_p$ and $2/3\lambda_p$ away from the position of the platform (Equation 55).

Critical wave selection irrespective of cell size

In section 5.6, it was discussed that grid convergence could not be obtained for the incipient point. Based on the results, a maximum error for the incipient point of $1/15\lambda_p$ could be estimated. Taking this error into account as a safety factor on the limits of the region near the platform in which breaking waves need to be considered, leads to

$$F_{\text{T}} = max \quad at \begin{cases} -\dfrac{6}{15}\lambda_p + x_{inc} < x_{\text{T}}, & max(\eta_{inc}) \\ \dfrac{11}{15}\lambda_p + x_{inc} > x_{\text{T}}, & max(\eta_{inc}) \cup max(\Gamma) \end{cases}. \tag{56}$$

Presenting the critical range for the onset of wave breaking

In subsection 4.2 it was found that wave overturning can take place directly after onset of breaking or within a distance of $1/5\lambda_p$ behind the position with the onset of breaking. In subsection 4.2 little difference was observed for the maximum surface elevation between breaking onset and wave overturning. Therefore the following critical wave selection range is presented for breaking onset

$$F_{\text{T}} = max \quad at \begin{cases} -\dfrac{9}{15}\lambda_p + x_{B85} < x_{\text{T}}, & max(\eta_{B85}) \\ \dfrac{11}{15}\lambda_p + x_{B85} > x_{\text{T}}, & max(\eta_{B85}) \cup max(\Gamma) \end{cases}, \tag{57}$$

with η_{B85} the maximum surface elevation measured at the position with the onset of breaking.

Wave screening range potential flow solver

From subsection 4.3 it was concluded that the error for the surface elevation was minimal at breaking onset. OceanWave3D overestimates the surface elevation compared to OpenFOAM. It was also observed that the onset of breaking in OpenFOAM could take place in a region of $-1/3\lambda_p$ to $1/15\lambda_p$ around the position with onset of breaking in OceanWave3D. From subsection 4.3 it was found that the breaking index could not reliably be found with the results of OceanWave3D. Therefore the range of critical wave selection for maximum platform forces becomes

$$F_{\text{T}} = max \quad at \begin{cases} -\dfrac{2}{3}\lambda_p + x_{B85} < x_{\text{T}}, & max(\eta_{B85}) \\ \lambda_p + x_{B85} > x_{\text{T}}, & max(\eta_{B85}) \end{cases}, \tag{58}$$

with x_{B85} the position of the onset of breaking and η_{B85} the maximum surface elevation at that position in OceanWave3D.

Discussion screening range

A wave selection procedure was discussed to identify the wave in simulation results of OceanWave3D that leads to the maximum force on a platform in a 2D setup of OpenFOAM. Wave selection requires the use of OpenFOAM to obtain the breaking index from undisturbed (without structure) wave simulations. An improved wave breaking model in OceanWave3D could make it possible to perform wave selection with OceanWave3D alone, which would make the selection procedure significantly more efficient.

6 Conclusion

The objective of this research was to find which wave selected from a sea state leads to the largest hydrodynamic loads on a 2D representation of a monopile inspection platform. It was found that the wave with the highest surface elevation and the largest breaking index leads to the largest hydrodynamic loads if it overturns within a distance of approximately $1/3\lambda_p$ before the location of the platform, with λ_p the wave length associated with the peak frequency of the spectrum. This leads to the following wave selection range for breaking waves in OceanWave3D

$$-\frac{2}{3}\lambda_p + x_{B85} < x_{\text{T}} < \lambda_p + x_{B85},$$

with x_{B85} the location of breaking onset and x_{T} the location of the structure. Waves with the highest surface elevation measured at the position of the onset of breaking are selected. All waves selected need to be simulated in OpenFOAM without structure to determine the breaking index, incipient point and maximum free surface particle velocity of the waves, because reliable estimates of these parameters from the OceanWave3D results could not be obtained. The horizontal location of maximum free surface particle velocity is important as there is a phase shift of approximately $1/15$ to $1/10\lambda_p$ with the position of the platform that experiences maximum platform forces. The incipient point is of importance as there is a phase shift between the platform position with a force maximum and the incipient point location of approximately $1/15\lambda_p$. The breaking index is a reliable predictor for which wave yields the maximum free surface particle velocities. As a converged solution for the maximum force on the platform could not be found in the grid sensitivity study, a validation experiment is needed to determine an adequate cell size for the OpenFOAM simulations. The lack of grid convergence could be caused by the shifting of the point of overturning, or by the chaotic nature of the wave breaking process, among other reasons.

The loads on the platform follow a pattern in time and space for all distances between platform position and incipient point of the breaking waves: a maximum run-up velocity is measured along the wall, a maximum local pressure is measured in the corner between platform and wall, a maximum force is measured shortly after the local pressure is at maximum, and, finally, a maximum overturning moment on the platform is measured. The first impact is observed in the corner between the wall and the platform. Therefore a platform placement with an opening between platform and wall may result in smaller loads. This opening could be considered a ventilation gap as described in Almeida and Hofland, 2021. The relation between the opening and the maximum loads is a matter of further research. Additionally it is unknown if a platform reaches its stress limit state due to the maximum local pressure, the maximum force or the maximum moment. This is matter for future study.

There seems to be a good relation between the free surface particle velocities for the undisturbed breaking wave and the measured platform Force. No (good) relation was found for the run-up velocity at the wall and the loads on the platform. It is estimated that the run-up thickness and the water particle accelerations are of importance as these have an influence on the added mass of the impact and therefore the loads on the platform. It is advised for run-up studies to measure the run-up thickness besides the run-up height with and without the presence of a platform - a maximum run-up height may not result in the largest platform forces.

The force on the platform during a wave impact can be approximately 6.5 times higher than the force with the platform positioned at the incipient point of the breaking wave. The setup was done in 2D without the effects of air compression, turbulence, and wave reflection. The 2D to 3D scale up relations with different physical settings may result in different loads. However the loads are estimated to remain significant because that was also found in Bos and Wellens, 2021. There seems to be an optimum direction of the free surface particle velocities just before impact to obtain the maximum force on the platform. The work has been done for a single storm event and for a slope of 1:21. More slopes and different storm settings need to be investigated.

The novel method for determining the breaking index with a virtual incipient point for irregular waves is verified with the results from Varing et al., 2021. However, the RMS error of the breaking index in our work is higher compared to the results from Varing et al., 2021. It must be verified if this is due to the nature of irregular waves, due to numerical errors in OpenFOAM, or due to the method of determining the breaking index with a virtual incipient point.

Oceanwave3D uses a user defined parameter γ for breaking wave energy removal. It is highly recommended to replace this value with the kinematic breaking criterion. A breaking criterion higher than one corresponds to theoretical wave overturning and $B = 0.85$ corresponds to the onset of breaking. Therefore, it is advised to keep the default setting of the newly defined breaking filter parameter (B) at 1.

Because of the difference in surface elevation between OceanWave3D and OpenFOAM before, during and after breaking, the correctness of the surface elevation in OceanWave3D after the activation of the Savitzky-Golay filter for wave breaking must be further investigated by means of a physical experiment.

Acknowledgements

We would like to thank Marnix Bockstael and Mike Blom for giving us fresh ideas and different perspectives on the subject.

References

Aggarwal, Ankit et al. (Nov. 2020). “Properties of breaking irregular waves over slopes”. In: *Ocean Engineering* 216. ISSN: 00298018. DOI: 10.1016/j.oceaneng.2020.108098.

Alberello, Alberto and Alessandro Iafrati (June 2019). “The velocity field underneath a breaking rogue wave: Laboratory experiments versus numerical simulations”. In: *Fluids* 4 (2). ISSN: 23115521. DOI: 10.3390/fluids4020068.

Almeida, Ermano De and Bas Hofland (2021). “Standing wave impacts on vertical hydraulic structures with overhangs for varying wave fields and configurations JOURNAL OF COASTAL AND HYDRAULIC STRUCTURES Standing wave impacts on vertical hydraulic structures with overhangs for varying wave fields and configurations”. In: 1, p. 10. DOI: 10.48438/jchs.2021.0010. URL: https://doi.org/10.48438/jchs.2021.0010.

Andersen, Thomas, ; Lykke, and Michael Brorsen (2007). *Aalborg Universitet Horns Rev II, 2D-Model Tests Impact Pressures on Horizontal and Cone Platforms from Irregular Waves*.

Andersen, Thomas Lykke et al. (Feb. 2011). “LOADS ON WIND TURBINES ACCESS PLATFORMS WITH GRATINGS”. In: *Coastal Engineering Proceedings* 1 (32), p. 65. ISSN: 0589-087X. DOI: 10.9753/icce.v32.structures.65.

Barthelemy, X. et al. (2018). “On a unified breaking onset threshold for gravity waves in deep and intermediate depth water”. In: *Journal of Fluid Mechanics* 841, 463–488. DOI: 10.1017/jfm.2018.93.

Bos, R. W. and P. R. Wellens (2021). “Fluid structure interaction between a pendulum and focused breaking waves”. In: *Physics of Fluids* 33.6. ISSN: 10897666. DOI: 10.1063/5.0054426.

Bredmose, H. and N. G. Jacobsen (2011). “Vertical wave impacts on offshore wind turbine inspection platforms”. In: *Proceedings of the International Conference on Offshore Mechanics and Arctic Engineering - OMAE* 5, pp. 645–654. DOI: 10.1115/OMAE2011-49785.

Bunnik, Tim, Jule Scharnke, and Erik-Jan De Ridder (2019). *EFFICIENT INDICATORS FOR SCREENING OF RANDOM WAVES FOR WAVE IMPACTS ON A JACKET PLATFORM AND A FIXED OFFSHORE WIND TURBINE*.

Craciunescu, Constantin Cosmin and Marios Christou (June 2020). “Wave breaking energy dissipation in long-crested focused wave groups based on JONSWAP spectra”. In: *Applied Ocean Research* 99. ISSN: 01411187. DOI: 10.1016/j.apor.2020.102144.

Damsgaard, Mathilde L, Helge Gravesen, and Thomas Lykke Andersen (2007). “Design Loads on platforms on Offshore wind Turbine Foundations with respect to vertical wave Run-up”. In.

Derakhti, M., M. L. Banner, and J. T. Kirby (Feb. 2018). “Predicting the breaking strength of gravity water waves”. In: URL: http://arxiv.org/abs/1802.03586.

Duncan, James H. (1983). “The breaking and non-breaking wave resistance of a two-dimensional hydrofoil”. In: *Journal of Fluid Mechanics* 126, 507–520. DOI: 10.1017/S0022112083000294.

Engsig-Karup, A. P., H. B. Bingham, and O. Lindberg (Apr. 2009). “An efficient flexible-order model for 3D nonlinear water waves”. In: *Journal of Computational Physics* 228 (6), pp. 2100–2118. ISSN: 10902716. DOI: 10.1016/j.jcp.2008.11.028.

Eça L., Hoekstra M. (2014). “A procedure for the estimation of the numerical uncertainty of CFD calculations based on rid refinement studies”. In: *Journal of Computational Physics* 262, pp. 103 –130. ISSN: 10902716.

Filip, Grzegorz P., Wenzhe Xu, and Kevin J. Maki (2020). “A method for the prediction of extreme wave loads on a fixed platform”. In: *Applied Ocean Research* 97.February, p. 101993. ISSN: 01411187. DOI: 10.1016/j.apor.2019.101993. URL: https://doi.org/10.1016/j.apor.2019.101993.

Garborg, Karsten et al. (2019). “Re-Analysis of Run-Up Levels for Slender Monopiles”. In: *International Journal of Ocean and Coastal Engineering* 02.01n02, p. 1950002. ISSN: 2529-8070. DOI: 10.1142/s2529807019500027.

Gourvenec, Susan and Rebecca Sykes (2021). *Offshore wind turbines could number 30,000 by 2030 – new ideas in ocean engineering are needed to install them*. URL: https://theconversation.com/offshore-wind-turbines-could-number-30-000-by-2030-new-ideas-in-ocean-engineering-are-needed-to-install-them-162618.

Grue, John and Bodgan Osyka (2021). “Runup on a vertical column in strong water wave events”. In: *Coastal Engineering* 163.June 2020, p. 103775. ISSN: 03783839. DOI: 10.1016/j.coastaleng.2020.103775. URL: https://doi.org/10.1016/j.coastaleng.2020.103775.

Howlermagazine (2018). *The Science of Shipstern Bluff | Tasmania’s Big Wave Surfing Break*. https://www.pressreader.com/costa-rica/howler-magazine/20180201/281668255432035. [Online; accessed 8-december-2022].

Jacobsen, Niels G., David R. Fuhrman, and Jørgen Fredsøe (2012). “A wave generation toolbox for the open-source CFD library: OpenFoam®”. In: *International Journal for Numerical Methods in Fluids* 70.9, pp. 1073–1088. DOI: https://doi.org/10.1002/fld.2726. eprint: https://onlinelibrary.wiley.com/doi/pdf/10.1002/fld.2726. URL: https://onlinelibrary.wiley.com/doi/abs/10.1002/fld.2726.

Korobkin, A. A. (Aug. 2007). “Second-order Wagner theory of wave impact”. In: *Journal of Engineering Mathematics* 58 (1-4), pp. 121–139. ISSN: 00220833. DOI: 10.1007/s10665-006-9105-7.

Kurnia, R. and E. van Groesen (2014). “High order Hamiltonian water wave models with wave-breaking mechanism”. In: *Coastal Engineering* 93 (1), pp. 55–70. ISSN: 03783839. DOI: 10.1016/j.coastaleng.2014.08.002.

Ma, Yuxiang et al. (2020). “Experimental study of plunging solitary waves impacting a vertical slender cylinder”. In: *Ocean Engineering* 202.February, p. 107191. ISSN: 00298018. DOI: 10.1016/j.oceaneng.2020.107191. URL: https://doi.org/10.1016/j.oceaneng.2020.107191.

McAllister, M. L. et al. (2018). “Laboratory recreation of the Draupner wave and the role of breaking in crossing seas”. In: *Journal of Fluid Mechanics* 860, pp. 767–786. ISSN: 14697645. DOI: 10.1017/jfm.2018.886.

Moideen, Rameeza et al. (2020). “Numerical Simulation and Analysis of Phase-Focused Breaking and Non-Breaking Wave Impact on a Fixed Offshore Platform Deck”. In: *Journal of Offshore Mechanics and Arctic Engineering* 142.5, pp. 1–8. ISSN: 1528896X. DOI: 10.1115/1.4046285.

Paulsen, Bo Terp, Henrik Bredmose, and Harry B. Bingham (Apr. 2014). “An efficient domain decomposition strategy for wave loads on surface piercing circular cylinders”. In: *Coastal Engineering* 86, pp. 57–76. ISSN: 03783839. DOI: 10.1016/j.coastaleng.2014.01.006.

Paulsen, Bo Terp et al. (2019). “Probability of wave slamming and the magnitude of slamming loads on offshore wind turbine foundations”. In: *Coastal Engineering* 143.April 2018, pp. 76–95. ISSN: 03783839. DOI: 10.1016/j.coastaleng.2018.10.002. URL: https://doi.org/10.1016/j.coastaleng.2018.10.002.

PENG, Zhong, Peter Wellens, and Tim Raaijmakers (July 2012). “3-D Numerical Modeling of Wave Run-Up on Monopiles”. In: vol. 5. DOI: 10.1115/OMAE2012-83858.

Ramirez, J. et al. (2013). “Large scale model test investigation on wave run-up in irregular waves at slender piles”. In: *Coastal Engineering* 72, pp. 69–79. ISSN: 03783839. DOI: 10.1016/j.coastaleng.2012.09.004.

Stansberg, Carl Trygve (May 2020). “Wave front steepness and influence on horizontal deck impact loads”. In: *Journal of Marine Science and Engineering* 8 (5). ISSN: 20771312. DOI: 10.3390/JMSE8050314.

Stansell, Paul and Colin Macfarlane (2019). *Experimental Investigation of Wave Breaking Criteria Based on Wave Phase Speeds*.

SurferToday (2019). *The Science of Shipstern Bluff | Tasmania’s Big Wave Surfing Break*. https://www.youtube.com/watch?v=zUsNjR-rhnA&ab_channel=SurferToday. [Online; accessed 1-december-2022].

Tai, Bing et al. (2019). “Experimental investigation of impact forces induced by plunging breakers on a vertical cylinder”. In: *Ocean Engineering* 189.August, p. 106362. ISSN: 00298018. DOI: 10.1016/j.oceaneng.2019.106362. URL: https://doi.org/10.1016/j.oceaneng.2019.106362.

Tang, Ye et al. (June 2020). “Effects of Spilling and Plunging Type Breaking Waves Acting on Large Monopile Offshore Wind Turbines”. In: *Frontiers in Marine Science* 7. ISSN: 22967745. DOI: 10.3389/fmars.2020.00427.

Varing, Audrey et al. (Mar. 2021). “A new definition of the kinematic breaking onset criterion validated with solitary and quasi-regular waves in shallow water”. In: *Coastal Engineering* 164. ISSN: 03783839. DOI: 10.1016/j.coastaleng.2020.103755.

Von Karman, T. (1929). “"The impact of seaplane floats during landing,"” in.

Wagner, Herbrt (Nov. 1932). “Über Stoß- und Gleitvogänge an der Oberfläche von Flüssigkeiten”. In: *ZAMM - Journal of Applied Mathematics and Mechanics / Zeitschrift für Angewandte Mathematik und Mechanik* 12, pp. 193 –215. DOI: 10.1002/zamm.19320120402.

Zhang, Zhenyu, Tongshun Yu, and Zishuai Zhao (Oct. 2022). “Wave run-up on composite bucket foundation due to random waves: Model tests and prediction formulae”. In: *Coastal Engineering* 177. ISSN: 03783839. DOI: 10.1016/j.coastaleng.2022.104177.